

1

2 **Sensitivity of the WRF-Chem v4.4 ozone, formaldehyde, and their precursors**
3 **simulations to multiple bottom-up emission inventories over East Asia during the**
4 **KORUS-AQ 2016 field campaign**

5

6 Kyoung-Min Kim¹, Si-Wan Kim^{2*}, Seunghwan Seo¹, Donald R. Blake³, Seogju Cho⁴,
7 James H. Crawford⁵, Louisa K. Emmons⁶, Alan Fried⁷, Jay R. Herman^{8,9}, Jinkyu Hong¹,
8 Jinsang Jung¹⁰ Gabriele G. Pfister⁶, Andrew J. Weinheimer⁶, Jung-Hun Woo¹¹, and
9 Qiang Zhang¹²

10

11 ¹Department of Atmospheric Sciences, Yonsei University, Seoul, South Korea

12 ²Irreversible Climate Change Research Center, Yonsei University, Seoul, South Korea

13 ³Department of Chemistry, University of California at Irvine, Irvine, CA, US

14 ⁴Seoul Metropolitan Government Research Institute of Public Health and
15 Environment, Gyeonggi-do, South Korea

16 ⁵NASA Langley Research Center, Hampton, VA, US

17 ⁶National Center for Atmospheric Research, Boulder, CO, US

18 ⁷Institute of Arctic and Alpine Research, University of Colorado, Boulder, CO, US

19 ⁸NASA Goddard Space Flight Center, Greenbelt, MD, US

20 ⁹University of Maryland Baltimore County, Baltimore, MD, USA

21 ¹⁰Korea Research Institute of Standards and Science, Daejeon, South Korea

22 ¹¹Department of Advanced Technology Fusion, Konkuk University, Seoul, South
23 Korea

24 ¹²Department of Earth System Science, Tsinghua University, Beijing, China

25

26

27 *To whom correspondence should be addressed. E-mail: siwan.kim@yonsei.ac.kr

28

29 Date: ~~0112/1201/20243~~

1 **Abstract**

2 In this study, the WRF-Chem v4.4 model was utilized to evaluate the sensitivity of O₃
3 simulations with three bottom-up emission inventories (EDGAR-HTAP v2, v3, and
4 KORUS v5) using surface and aircraft data in East Asia during the Korea-United States
5 Air Quality (KORUS-AQ) campaign period in 2016. All emission inventories were
6 found to reproduce the diurnal variations of O₃ and its main precursor NO₂ as compared
7 to the surface monitor data. However, the spatial distributions of the daily maximum 8-
8 hour average (MDA8) O₃ in the model do not completely align with the observations.
9 The model MDA8 O₃ had a negative (positive) bias north (south) of 30°N over China.
10 All simulations underestimated the observed CO by 50-60% over China and South
11 Korea. In the Seoul Metropolitan Area (SMA), EDGAR-HTAP v2, v3, and KORUS v5
12 simulated the vertical shapes and diurnal patterns of O₃ and other precursors effectively,
13 but the model underestimated the observed O₃, CO and HCHO concentrations. Notably,
14 the model aromatic VOCs were significantly underestimated with the three bottom-up
15 emission inventories, although the KORUS v5 shows improvements. The model
16 isoprene estimations had a positive bias relative to the observations, suggesting that the
17 Model of Emissions of Gases and Aerosols from Nature (MEGAN) version 2.04
18 overestimated isoprene emissions. Additional model simulations were conducted by
19 doubling CO and VOC emissions over China and South Korea to investigate the causes
20 of the model O₃ biases and the effects of the long-range transport on the O₃ over South
21 Korea. The doubled CO and VOC emission simulations improved the model O₃
22 simulations for the local emission dominant case, but led to the model O₃
23 overestimations for the transport dominant case, which emphasizes the need for
24 accurate representations of the local VOC emissions over South Korea.

1 **1. Introduction**

2 Air pollutants not only harm human health but also affect radiative balance, resulting
3 in climate change (Anenberg et al., 2018; Franklin et al., 2015; Lee et al., 2014;
4 Manning and von Tiedemann, 1995; Rosenzweig et al., 2008; Wild et al., 2001).
5 Anthropogenic activities are the primary source of air pollutant emissions, which have
6 significant temporal and spatial variability. Chemical transport models (CTMs) use
7 bottom-up emission data to simulate ambient concentrations of air pollutants. CTMs
8 then process these emissions, tracking their impact through chemistry, transport, and
9 loss through deposition (Zhong et al., 2016). Therefore, sensitivity evaluations of CTMs
10 to anthropogenic emission data are an essential part of atmospheric modeling research.

11 Several bottom-up emission inventories are available for chemical modeling of
12 Asia, including the Multi-resolution Emission Inventory for China (MEIC), Regional
13 Emission inventory in Asia (REAS), and Emissions Database for Global Atmospheric
14 Research-Hemispheric Transport of Air Pollution (EDGAR-HTAP). Since 2010,
15 Tsinghua University has developed the high-resolution MEIC emission inventory for
16 China and updated the data to the v1.3, providing anthropogenic emissions by sector
17 and species from 2008 to 2017 (Zheng et al., 2018). REAS provides emission data in
18 Asia from 1950 to 2015 (Kurokawa and Ohara, 2020). In Europe, EDGAR-HTAP has
19 been developed and widely used for CTM simulations from global to regional scale
20 (Kim et al., 2021; Sharma et al., 2017; Sicard et al., 2021). Recently, EDGAR-HTAP
21 v3 has been published, covering 19 years from 2000 to 2018 compared to only two
22 years (2008 and 2010) in the version 2 data (Crippa et al., 2023). Zhong et al. (2016)
23 compared REAS with EDGAR in July, 2007 over China, while Saikawa et al. (2017)
24 compared 5 emission inventories including REAS, EDGAR, MEIC in China, without

1 validation. As bottom-up emission inventories are continuously updated for recent years,
2 there is an ongoing need to evaluate new emissions data.

3 The Ministry of Environment (MOE) in South Korea and National Aeronautics and
4 Space Administration (NASA) in the U.S. conducted the Korea-United States Air
5 Quality (KORUS-AQ) campaign in May-June 2016. The campaign provided a variety
6 of data sets, including ground-based and airborne observations, useful for the validation
7 of model simulations. The KORUS emissions, developed by Konkuk University, were
8 used by many modeling teams to simulate the air pollutant concentrations during the
9 campaign period. Numerous modeling studies were conducted for this period including
10 validations of CTM results with diverse observation datasets. Miyazaki et al. (2019)
11 adjusted emission inventories using various satellite data sets and Model for
12 Interdisciplinary Research on Climate with chemistry (MIROC-Chem), resulting
13 improved simulations of tropospheric O₃. Goldberg et al. (2019) reported
14 underestimations of NO_x emissions in South Korea, particularly in Seoul. Souri et al.
15 (2020) also revealed the same issue in South Korea and conducted analysis of the
16 sensitivity of O₃ formation to adjustments in NO_x and volatile organic compound (VOC)
17 emission derived from inverse modeling. Tang et al. (2019) revealed negative biases of
18 simulated CO concentrations in East Asia by utilizing satellite data and the Community
19 Atmosphere Model with Chemistry (CAM-Chem). Choi et al. (2022) modified
20 anthropogenic VOC emissions through the inverse modeling using satellite HCHO
21 observations with the Goddard Earth Observing System with Chemistry (GEOS-Chem),
22 which reduced O₃ and HCHO biases.

23 Recently, the updated version of bottom-up emission inventories and CTMs have
24 become available for the air pollution modeling studies in East Asia. In this study, we

1 selected the EDGAR-HTAP versions 2 and 3, and KORUS version 5 emission data and
2 used the Weather Research and Forecasting model coupled with Chemistry (WRF-
3 Chem) version 4.4 for intercomparison of the three emissions data sets, aiming to
4 understand the status of precursor emissions from bottom-up emission inventories and
5 their uncertainties, which may impact the O₃ formations in the model. O₃ and its major
6 precursors were selected for model evaluation and the model results were evaluated
7 with surface observation data in China and South Korea and aircraft data acquired over
8 the South Korean peninsula and surrounding waters.

9 The manuscript is organized as follows. The data and methods section introduces
10 emission inventories, the numerical model, and meteorological and chemical
11 observations. The results section evaluates the model's meteorology and chemistry
12 using routine surface observations over China and South Korea. Subsequently, the
13 model results employing three bottom-up emission inventories are compared with
14 sophisticated chemical observations obtained during the KORUS-AQ field campaign,
15 primarily over South Korea. This comparison summarized the model's performance
16 with each emission inventory. In the discussion section, strategies to enhance surface
17 O₃ simulations, along with accurate precursor simulations, are proposed based on
18 various emission scenarios for urban and regional areas over China and South Korea.
19 The summary and conclusion section follow, providing overview of the key findings
20 and conclusions drawn from the study.

21

1 **2. Data and Methods**

2 **2.1. WRF-Chem model configurations**

3 In this study, we utilized the WRF-Chem v4.4, which was developed by the National
4 Oceanic and Atmospheric Administration (NOAA) and National Center for
5 Atmospheric Research (NCAR), to simulate meteorological variables and chemical
6 species in the atmosphere (Grell et al., 2005). The WRF-Chem v4.4 includes N_2O_5
7 heterogeneous chemistry that consists of several chemical reactions related with ClNO_2
8 and N_2O_5 reactions, resulting in nitrate aerosol. The reactions are incorporated in
9 Secondary Organic Aerosol-Volatility Basis Set (SOA-VBS) with Regional
10 Atmospheric Chemistry Mechanism (RACM) chemistry option (chem = 108) in WRF-
11 Chem (Li et al., 2016).

12 We set 59 vertically customized eta (η) levels as vertical layers. The model's first
13 layer height is approximately 40 m above ground level for the entire domain. The
14 model's vertical layers are designed to include about 17 layers under 1.5 km to simulate
15 planetary boundary layer chemistry and near surface vertical distribution in detail. The
16 horizontal resolution is $28 \times 28 \text{ km}^2$. The simulations in this study start at 12 UTC on
17 April 24 and end at 12 UTC on June 11. The model meteorology restarts every 12 UTC
18 (9 PM local time in South Korea) to minimize numerical errors. After the first 7 days
19 of model initiation (spin-up), we analyzed the model results from May 1 to June 10. We
20 used China standard time (+8 UTC) and Korea standard time (+9 UTC) for evaluations
21 with observations. The model physics, chemistry, and aerosol schemes are summarized
22 in Table S1 with corresponding references. The Global Forecast System (GFS) Final
23 (FNL) analysis data are used for meteorological input and boundary conditions. The
24 Community Atmosphere Model with Chemistry (CAM-Chem) output is used for

1 chemical boundary conditions (<https://rda.ucar.edu/datasets/ds313.7/>) (Buchholz et al.,
2 2019; Emmons et al., 2020). We used the Model of Emissions of Gases and Aerosols
3 from Nature (MEGAN) v2.04 to calculate biogenic emissions (Guenther et al., 2006).
4 We did not account for fire emissions because of small impact on air quality simulations
5 during the KORUS-AQ campaign period (Park et al., 2021). In our sensitivity
6 simulation with the Fire INventory from NCAR (FINN) v2.5 fire emissions
7 (Wiedinmyer et al., 2022), a marginal increase in the simulated averaged daily
8 maximum 8-hour average (MDA8) O₃ of approximately 1 ppbv (1.6 %) was noted in
9 China (Supporting information, Figure S1).

10

11 **2.2. The model simulations using different anthropogenic emissions**

12 **2.2.1. Bottom-up emission data**

13 EDGAR-HTAP v2, v3, and KORUS v5 anthropogenic bottom-up emission inventories
14 are compared with respect to their spatial distribution and total amount in Figure 1 and
15 Table S2. We applied the same diurnal factor for all three emissions data by species,
16 following the diurnal patterns for the Los Angeles Basin as in Kim et al. (2016) (also
17 see Figure S2).

18 EDGAR-HTAP v2 provides 2-dimensional emissions of CH₄, CO, SO₂, NO_x (NO
19 + NO₂), total non-methane volatile organic compound (NMVOC), NH₃, PM₁₀, PM_{2.5},
20 BC, and OC in 2008 and 2010 with a horizontal resolution of 0.1° x 0.1°. We used 2010
21 data since it is the most recent data available. The data are partitioned by each sector
22 and its sources such as air, ships, energy, industry, transport, residential, and agriculture
23 (https://edgar.jrc.ec.europa.eu/dataset_htap_v2). For East Asia, it included data from

1 the Model Inter-Comparison Study for Asia (MICS-Asia) and REAS v2.1. In South
2 Korea, it adopted data from the Clean Air Policy Support System (CAPSS) (Janssens-
3 Maenhout et al., 2015), and the underlying emission data had an original horizontal
4 resolution of $0.25^{\circ} \times 0.25^{\circ}$ over East Asia, which is resampled to $0.1^{\circ} \times 0.1^{\circ}$ resolution
5 by raster resampling and aggregation. The speciated EDGAR-HTAP v2 VOC data were
6 obtained through the WRF-Chem site ([https://www.acom.ucar.edu/wrf-
7 chem/download.shtml](https://www.acom.ucar.edu/wrf-chem/download.shtml)) in the *anthro_emiss* program with the Model for Ozone and
8 Related chemical Tracers (MOZART) species (Supporting Information, Table S3). The
9 *anthro_emiss* program converts the EDGAR-HTAP v2 data into $28 \times 28 \text{ km}^2$ grid by
10 the RACM chemical species (Supporting Information, Table S4). It mapped the
11 MOZART volatile organic compounds (VOC) species into the RACM VOC species
12 (See the detailed equations in Supporting Information, Table S5) (Li et al., 2014;
13 Emmons et al., 2010).

14 The EDGAR-HTAP v3 is extended to much longer time scale than the previous
15 version EDGAR-HTAP (v2). The EDGAR-HTAP v3 covers 2000 to 2018 with a more
16 detailed horizontal resolution (https://edgar.jrc.ec.europa.eu/dataset_htap_v3) (Crippa
17 et al. 2023). While EDGAR-HTAP v2 uses MICS-Asia, only the REAS data are used
18 in China and India in the EDGAR-HTAP v3. It adopts the CAPSS-Konkuk University
19 (CAPSS-KU) data for South Korea and emission data provided by the Japanese
20 government for Japan. We chose the data for 2016, according to the KORUS-AQ
21 campaign period. Because the original EDGAR-HTAP v3 data provide VOC as total
22 NMVOC with the unit of ton/month, we distributed the total NMVOC to MOZART
23 VOC species with the ratio of each VOC species to total NMVOC from EDGAR-HTAP
24 v2 in *anthro_emiss* program. Then, the assigned EDGAR-HTAP v3 data were again

1 converted to the RACM.

2 The KORUS v5 emission data represent 2016 in China and 2015 in other regions.
3 The Comprehensive Regional Emissions Inventory for Atmospheric Transport
4 Experiment (CREATE) v2.3 data from 2015 were used and the ship emissions from
5 CAPSS were added near the coastal region in South Korea (Jang et al., 2020; Woo et
6 al., 2012). The CREATE is originally developed by combining REAS, MEIC, Japan
7 Auto-Oil Program emission inventory (JATOP), and Korean Clear Air Policy Support
8 System (CAPSS). The NMVOC species from KORUS v5 were mapped following the
9 Statewide Air Pollution Research Center (SAPRC-99) mechanism, and we also
10 assigned the SAPRC-99 species to RACM (Carter, 2000) (Supporting information,
11 Table S5-6).

12 Figure 1 shows the spatial distribution of NO, CO, and TOL (toluene + less reactive
13 aromatics defined in RACM, see Table S4) emissions in May for each inventory. The
14 NO_x emissions were assumed to be emitted as NO. The major cities in China and South
15 Korea had relatively high NO, CO, and TOL emissions, which are precursors affecting
16 O₃ formation. We define three boxes representing Eastern China, South Korea, and the
17 Seoul metropolitan area (SMA) and calculated the emissions (see Table S2). In South
18 Korea including SMA, EDGAR-HTAP v3 had the largest NO_x emission among the
19 emission inventories. The KORUS v5 has lower NO_x emissions in Eastern China by
20 46% and 39% compared to EDGAR-HTAP v2 and v3, respectively. The CO emission
21 was the lowest in EDGAR-HTAP v2 in South Korea, being 56% (69%) lower than that
22 in KORUS v5 (EDGAR-HTAP v3). KORUS v5 showed the highest CO emissions in
23 SMA though EDGAR-HTAP v3 showed more CO emissions in South Korea. However,
24 KORUS v5 had the smallest CO emissions in China, being 7% (9%) lower than that in

1 EDGAR-HTAP v2 (v3). The TOL emissions ~~from~~in KORUS v5 is higher than those
2 ~~from~~in EDGAR-HTAP v2 (EDGAR-HTAP v3) by 176% (98%) in China. The relative
3 difference of TOL between KORUS v5 and EDGAR-HTAP v2 (EDGAR-HTAP v3) is
4 larger in South Korea by 263%. On the other hand, EDGAR-HTAP v3 ~~has~~ve ~~the~~
5 ~~largest~~ total NMVOC emissions over China than EDGAR-HTAP v2 and KORUS v5
6 by 38% and 27 %, respectively. These discrepancies ~~of~~in VOC emissions may lead to
7 a change in the NO_x/VOC-sensitive regime and O₃ production efficiency in South
8 Korea and China. The sensitivity of O₃ formation to NO_x emission has discrepancies
9 by its regime; a reduction in NO_x leads to a decrease in O₃ in the NO_x-limited regime,
10 while in the VOC-limited regime (or NO_x-saturated regime), it results in an increase in
11 O₃. This, which will be further discussed in section 3.2.

13 2.2.2. The model experiments

14 The model experiments are summarized in Table 1. The simulations using EDGAR-
15 HTAP v2, v3, and KORUS v5 emissions are named as EDV2, EDV3, and KOV5,
16 respectively. In this study, we found consistent underestimation of CO, HCHO, TOL,
17 and XYL for all emissions by -40% (\pm 2%), -25% (\pm 1%), -67% (\pm 21%), -53% (\pm
18 18%), respectively, compared to observations from the DC-8 in South Korea. Here TOL
19 and XYL are lumped species including toluene and xylene, respectively. This is in line
20 with the results reported by Park et al. (2021), who found that almost every model
21 underestimated CO. Underestimation of CO in East Asia is a well-known feature
22 revealed by many studies. For example, Gaubert et al. (2020) mentioned that CAM-
23 Chem underestimates CO during the KORUS-AQ campaign period and presented a CO

1 compensation method utilizing data assimilation with CO observations. Wada et al.
2 (2012) pointed out that EDGAR v4.1 underestimates anthropogenic CO emissions in
3 China by 45% compared to observation-based estimations of CO emissions. Moreover,
4 underestimation of VOC is also found for all anthropogenic emission inventories.
5 Kwon et al. (2021) estimated top-down emissions of anthropogenic VOCs utilizing
6 Geostationary Trace gas and Aerosol Sensor Optimization spectrometer (GeoTASO).
7 They found that top-down VOC emissions were up to 6.9 times higher than bottom-up
8 emissions (KORUS v5).

9 For all emission inventories in simulations with WRF-Chem, O₃ is underestimated
10 at most ground-based observation sites in South Korea. To figure out the potential
11 causes of negative biases of O₃ in South Korea, we conducted three additional model
12 simulations using EDGAR-HTAP v3 that shows the lowest bias of O₃ concentrations
13 compared to DC-8 than EDGAR-HTAP v2 and KORUS v5 over the SMA; the mean
14 biases are -16.9, -14.2, and -18.1 ppb with EDV2, EDV3, and KOV5, respectively. Two
15 simulations are with twice the anthropogenic CO and VOC emissions in China
16 (EDV3_Ch2) and South Korea (EDV3_Ko2), respectively, and the third simulation
17 uses double CO and VOC emissions in both China and South Korea (EDV3_ChKo2)
18 to investigate possible improvements in the simulated O₃ and CO from these emission
19 changes. To ~~propose the simulate possible~~ strategies to improve surface O₃ simulations
20 over China and South Korea, we incorporated 4 additional emission scenarios involving
21 the reduction of NO_x and/or VOC emissions over China. Specifically, we considered
22 the cases with a 50% reduction in NO_x emissions only, a 50% reduction in VOC
23 emissions only, a simultaneous 50% reduction in both NO_x and VOC emissions, and a
24 75% reduction in NO_x emissions only. For more details, refer to Section 4 (Discussion).

1

2 **2.3. Observations**

3 **2.3.1. Meteorological data**

4 The meteorological field that WRF-Chem reproduced is evaluated with the surface
5 synoptic observation (SYNOP) data operated by the World Meteorological
6 Organization (WMO) (<http://www.meteomanz.com>). Surface temperature, relative
7 humidity, and surface wind speed are adopted for model validation. As the SYNOP data
8 are provided every 3 or 6-hourly, we selected model data when the observation data are
9 available. There were 271 sites in China-Taiwan-Hongkong and 48 sites in South Korea.

10

11 **2.3.2. Ground-based observations**

12 The surface observation network used in this study was obtained from Airkorea in South
13 Korea and the China Ministry of Ecology and Environment (MEE) in China. The
14 Airkorea observation network provides 1-hourly measurements of NO₂, SO₂, CO, O₃,
15 PM₁₀, and PM_{2.5} at suburban, background, roadside, city, and port sites
16 (www.airkorea.or.kr). The concentrations of NO₂, CO, and O₃ are measured using the
17 chemiluminescent, non-dispersive infrared, and ultraviolet photometric methods,
18 respectively. In South Korea, there are indications of positive biases in NO₂ surface
19 observations, potentially resulting in overestimations of ~30%, particularly at suburban
20 sites in spring (Jung et al., 2017). The model data with 28 x 28 km² horizontal resolution
21 were linearly interpolated to the 365 sites in South Korea, and we selected NO₂, O₃, and
22 CO for model validation.

1 The Chinese observations were provided by MEE through the website
2 (beijingair.sinaapp.com). Surface NO₂ over China was measured using a molybdenum
3 converter, which has the potential for positive biases due to other NO₂-related oxidation
4 products (Dunlea et al., 2007). CO was measured using infrared absorption (Zhang and
5 Cao., 2015), and there were 1454 stations in China during the campaign period.

6 For validation of NO₂ and HCHO vertical column density, data from the Pandora
7 spectrometer were used, which the model reproduced with emission inventories at the
8 Olympic Park site (37.5232°N, 127.126°E). The HCHO data from Pandora is corrected
9 because of internal off-gasing to avoid positive biases (Spinei et al., 2021). At the same
10 observation site, surface NO₂ was also measured by a KENTEK NO_x analyzer with
11 photolytic method, and surface O₃ was measured using the same instrument. Ground-
12 based HCHO was measured using Aerodyne QCL. We compared the observed diurnal
13 cycle of vertical column and surface concentrations of NO₂ and HCHO with the model
14 simulations utilizing EDV2, EDV3, and KOV5. We also used ground-based VOC data
15 from gas chromatography flame ionization detector (GC-FID) operated by the Seoul
16 Research Institute of Public Health and Environment (SIHE).

17

18 **2.3.3. Aircraft data**

19 The DC-8 research aircraft, operated by NASA, performed multiple flight
20 measurements with a variety of measuring instruments. We utilized 1 minute interval
21 merged data of O₃, NO₂, CO, HCHO, and VOC along the 20 flight paths (Figure 2).
22 The nearest WRF-Chem grid is selected and then temporally and vertically interpolated
23 to the aircraft data using linear interpolation ~~method~~ to fully utilize the observations.

1 Atmospheric NO₂ and O₃ concentrations were measured using a 4-channel
2 chemiluminescence instrument, with an uncertainty of 100 pptv + 30% and 5 ppbv +
3 10%, respectively. CO concentrations were observed using a diode laser spectrometer,
4 with an uncertainty of 2% or 2 ppbv. The Compact Atmospheric Multi-species
5 Spectrometer (CAMS) was used to measure HCHO concentration, with a possible 3%
6 systematic error (Richter et al., 2015). We also utilized data from the Whole Air Sampler
7 (WAS) to analyze VOC species from different emission inventories (Colman et al.,
8 2001). In this study, we focused on DC-8 observations below a height of 2 km to
9 concentrate on planetary boundary layer (PBL) chemistry. The observation height was
10 determined by GPS altitude above ground level.

11

12 **3. Results**

13 **3.1. The model meteorology simulations**

14 The model temperature and relative humidity were compared with surface observations
15 in China and South Korea. The model-simulated temperature had a slight negative mean
16 bias of -0.91 °C (correlation coefficient R = 0.90) in China, with the largest negative
17 bias in southwestern China. In South Korea, the mean bias was -1.71 °C (R = 0.88). The
18 simulated relative humidity showed a negative bias of -20 to -10% in the North China
19 Plain (NCP) area and a positive bias of 10 to 20% in southwestern China. There was a
20 negative bias of relative humidity over the west coastal area and a positive bias of 10 to
21 20% at most observation stations in South Korea. The correlation coefficients between
22 the model relative humidity and observations were 0.85 and 0.76 for China and South
23 Korea, respectively. Overall, the comparisons showed decent model simulations of
24 meteorology. A negative temperature bias could result in a reduction of isoprene

1 emissions, as illustrated in Figure S3 of the Supporting Information, compared to the
2 estimates based on accurately simulated temperature ~~(Figure S3)~~.

3 During the KORUS-AQ campaign period, WRF-Chem accurately simulated the
4 daytime PBL height from a laser ceilometer (CL-31, Vaisala Inc., Finland) observed at
5 Yonsei University in Seoul, South Korea (Lee et al., 2019). But, Travis et al. (2022) has
6 indicated the possibility of PBL height underestimations by CTMs. Furthermore, due
7 to limitations of the instrument, the ceilometer has potential to inadequately estimate
8 nighttime PBL height. It is primarily attributed to the method based on aerosol gradients
9 (Jordan et al., 2020). Therefore, the interpretation of simulated nighttime concentrations
10 of air pollutants should be approached with caution. More analysis of meteorological
11 fields, including PBL height, can be found in the Supporting Information (Table S7 and
12 Figure S4-S5).

14 **3.2. Evaluations with routine surface chemical observational data**

15 The study compared simulated concentrations of O₃, NO₂, and CO with data from
16 routine surface observational networks (Table 2 and Figure 3-7). First, the diurnal
17 variations of the model O₃ using different emissions inventories were compared with
18 observations for each subregion (Table 2 and Figure 3). Overall, all emission
19 inventories successfully reproduced diurnal variations and absolute values of O₃ for
20 most regions, but there were notable discrepancies in several regions.

21 In the North China Plain (NCP) region, EDV2 led to a negative model O₃ bias (-12
22 ppb) with R=0.65, while EDV3 and KOV5 simulated O₃ better with reduced biases and
23 increased correlations (R=0.68-0.71). The high NO_x emissions relative to the VOC

1 emissions in NCP led to a low formaldehyde to NO₂ ratio (FNR) (<1), suggesting that
2 the NCP area is in a VOC-limited regime with all emission inventories (Table 3). Due
3 to the elevated reactive VOC emissions in EDV3 and KOV5 compared to EDV2, both
4 EDV3 and KOV5 show improved O₃ simulations. Similarly, EDV2 had a negative O₃
5 bias (-17 ppb) with R=0.62 in the Yangtze River Delta (YRD) area, but EDV3 and
6 KOV5 much improved the simulations, which was also observed in the Northeastern
7 China (NEC) area. However, the model O₃ concentrations based on the three emission
8 inventories were overestimated in the Sichuan-Chongqing-Guizhou (SCG) and
9 Southeastern China (SEC) area. In SCG and SEC, the WRF-Chem simulated higher
10 biogenic isoprene emissions compared to anthropogenic TOL and XYL emissions by
11 up to a factor of 10, leading to a high FNR (> 1). In Pearl River Delta (PRD), EDV2
12 showed the lowest bias (-0.3 ppb) compared to EDV3 and KOV5 because EDV3 and
13 KOV5 have elevated anthropogenic VOC emissions as well as enhanced biogenic
14 isoprene emissions under a VOC-limited regime (Table 3). In the suburban area of
15 Northern China (NOC), all emission inventories reasonably simulated hourly O₃
16 concentrations.

17 Averaged O₃ was well simulated in South Korea (KOR) with low biases (-1 to 0.7
18 ppb), but a negative bias appears over the Seoul metropolitan area (SMA) with all
19 emissions (-5.5 to -3.5 ppb) (Table 2). WRF-Chem simulations indicate SMA as a
20 highly NO_x-saturated region (FNR < 0.2), resulting in being VOC-sensitive for O₃
21 production. The underestimated model O₃ levels in this region suggests the possibility
22 of insufficient anthropogenic VOC emissions in SMA across all emission inventories
23 (Table 3). A detailed discussion will be provided in section 3.3.

24 The study also analyzed the mean values of MDA8 O₃ concentration at each site

1 and their spatial distributions for the entire campaign period (Figure 4). The spatial
2 distributions of the model MDA8 O₃ were not well correlated with those of the
3 observations. But, notable disparities were observed in simulating MDA8 O₃ when the
4 different emissions were used. For the north and eastern part of China including Beijing
5 and Shanghai, large negative biases disappear when using EDV3 and KOV5. KOV5
6 only shows a significant correlation with the surface MDA8 O₃ observations (including
7 929 sites) than EDV2 and EDV3 in China (0.43 versus 0.01, 0.20). The correlations
8 between the time series of the model MDA8 O₃ and observations varied at each site,
9 with about 40-60% of sites (depending on the emission inventories) showing a
10 correlation coefficient greater than 0.6 (see Supporting Information, Figure S6), and the
11 locations of these sites were scattered. The correlation slightly improved with hourly
12 O₃ concentrations instead of MDA8 O₃, with about 50-60% of sites having a correlation
13 coefficient greater than 0.6 (Supporting Information, Figure S6). For this metric, high
14 correlations occurred in pollution hot spots north of 30°N and the South Coast of China,
15 in which the ratio of HCHO to NO₂ (FNR) was much less than 1, suggesting VOC-
16 limited/NO_x-saturated chemical regime (Supporting Information, Figure S7). The
17 model MDA8 O₃ were underestimated for the pollution hot spots with a low HCHO to
18 NO₂ ratio located north of 30°N, suggesting a possibility of model underestimations of
19 anthropogenic VOC emissions causing model MDA8 O₃ biases at these sites. In
20 contrast, the simulated MDA8 O₃ was generally overestimated for sites south of 30°N
21 in which HCHO concentrations were high (Supporting Information, Figure S7). Zhang
22 et al. (2020) reported that simulated biogenic isoprene (ISO) from MEGAN was
23 overestimated compared to observation sites ~~under-south of~~ 35°N in China.

1 The EDV2 and EDV3 showed a positive NO₂ bias over the YRD, NCP, and PRD
2 regions, which include large cities in China (Table 2 and Figure 5-6). On the other hand,
3 EDV2 and EDV3 had small negative NO₂ biases in the NEC and NOC regions. All
4 models demonstrated reasonable NO₂ model performance in the SCG region, where
5 MDA8 O₃ was overestimated (Figure 3 and 5). In the YRD region, there were large
6 positive NO₂ biases with EDV2, EDV3, and KOV5 (ranging from 6.4 to 22.7 ppb). Liu
7 et al. (2021) reported that YRD is in a VOC-limited regime when using EDV2. The
8 findings indicated that a reduction in NO_x emissions led to an increase in O₃
9 concentrations, while a reduction in VOC emissions resulted in lower O₃ concentrations.
10 The O₃ in YRD can be attributed to the combined influence of higher anthropogenic
11 NO_x emissions and VOC originated from both anthropogenic and biogenic sources
12 (Figure S7). In contrast, KOV5 underestimated NO₂ in the NCP region, while EDV2
13 and EDV3 did not. All emissions showed significant discrepancies compared to NO₂
14 observations in the SEC area, with a low correlation coefficient (0.19 to 0.26). EDV3
15 showed the smallest bias of -1.9 ppb (-0.8 ppb) compared to EDV2 and KOV5 in South
16 Korea (SMA). The daily averaged NO₂ exhibited spatial distributions similar to MDA8
17 O₃ and CO (Figure 6). The slopes of regression between the three model simulations
18 and observations were 1.31, 1.03, and 0.8 for EDV2, EDV3, and KOV5, respectively,
19 in China. The correlation coefficients between the simulated NO₂ utilizing EDV2,
20 EDV3, and KOV5 and surface data were around 0.6 in China. EDV2, EDV3, and
21 KOV5 demonstrated good correlations with observations in South Korea (R = 0.69-
22 0.74). Correlation coefficient (R) was the highest with KOV5 in South Korea (R=0.74).

23 Likewise, the diurnal patterns of Ox (= NO₂ + O₃) are well simulated with all
24 emission inventories (Supporting Information, Figure S8). The spatial distribution and

1 diurnal patterns of Ox are similar to O₃ except YRD (Supporting Information, Figure
2 S9). In YRD, the overestimations of Ox with all emission inventories reveals that same
3 issue of NO₂ overestimations in Figure 5. Even though O₃ is well simulated in this
4 region, the negative impact of NO_x titration to O₃ formation is compensated with the
5 overestimated anthropogenic and biogenic VOC emissions as mentioned above.

6 The simulated CO was averaged at each site and compared with observations
7 during the KORUS-AQ campaign period (Figure 7). The three model results showed
8 similar spatial distributions to observations, indicating higher CO concentrations in the
9 NCP, YRD, and PRD regions than their surrounding areas. However, all simulations
10 failed to reproduce the abundance of CO, indicating large negative biases throughout
11 the country. The bias was larger in South Korea than in China.

12

13 **3.3. Evaluations with the airborne and special surface chemical observations** 14 **during KORUS-AQ**

15

16 **3.3.1. The aircraft observations**

17 Figure 2 shows the flight paths flown by the DC-8 during the KORUS-AQ campaign
18 period. In Table 4, we compare the model results for O₃, NO₂, CO, HCHO, TOL, XYL,
19 ETE (Ethene or OL2), and ISO with the corresponding observed values for all flight
20 tracks under 2 km height in South Korea. On average, the model underestimated O₃ by
21 15-18 ppb, with EDV3 exhibiting the lowest O₃ bias (-15.1 ppb) compared to EDV2
22 and KOV5 (-16.8 and -17.5 ppb, respectively). All emissions showed positive biases
23 for NO₂ (0.64 to 1.72 ppb), ETE (0.08 to 0.14 ppb), and ISO (0.1 to 0.11 ppb). However,
24 the model significantly underestimated CO, HCHO, TOL, and XYL for all three
25 emissions. Given the large spatial variability of air pollutants in South Korea, we also

1 sampled aircraft data from six regions (see Figure 2) and compared the three model
2 results with the aircraft observations under 2 km height (Figure 8).

3 The flight tracks that surveyed large power plants and factories in the Chungnam
4 region on a daily basis are shown in Figure S10 in the Supporting Information. The
5 largest negative model O₃ bias was observed over the Chungnam region, with a
6 difference of 38-41 ppb. Emission estimation uncertainties can be significant over this
7 region, where there are large point sources such as coal-burning power plants and
8 petrochemical industries. The model NO₂ agreed with the aircraft observations in SMA,
9 but it tends to overestimate the measurements in the other areas. There were substantial
10 model overestimations of NO₂ with EDV3 over the Chungnam and Busan areas, while
11 KOV5 showed the most reasonable model NO₂ simulations. The model CO near the
12 surface was underestimated in the entire domain, resulting in high negative model CO
13 biases relative to the aircraft observations across the six regions (Figure 8). We
14 additionally conducted [a](#) sensitivity test to investigate the contribution of CO to O₃
15 concentrations in SMA (Supporting information, Figure S11). Doubling CO emissions
16 in China did not significantly change O₃ concentrations at all levels under 2 km. Only
17 1.4 ppb of O₃ concentrations are changed on average during all flight observations.

18 We also evaluated the model HCHO, which can be formed by oxidation of other
19 VOCs but also directly emitted by anthropogenic sources, to investigate uncertainties
20 in anthropogenic VOC emissions. The model HCHO was underestimated by all
21 emission inventories for all subregions, with negative biases being evident in the SMA,
22 Yellow Sea, and Chungnam regions.

23 Other model VOC species, such as TOL, XYL, ETE, and ISO, were also analyzed.
24 These VOC species are classified by their chemical structures and reactivities in the

1 RACM (Stockwell et al., 1997) (Table S4). For example, TOL includes toluene and
2 relatively less reactive aromatics, while XYL includes xylene and more reactive
3 aromatics. The WAS data from DC-8 were lumped into RACM (Supporting
4 Information Table S8, Lu et al., 2013) and were compared with aircraft observations.
5 When the model TOL or XYL was compared with the observed toluene and xylene, the
6 model using KOV5 reasonably reproduced the observed concentrations (light gray bars
7 in Figure 8). However, the model TOL (even using KOV5) underestimated the observed
8 lumped TOL for most of the regions except for Busan (bars including the dark gray part
9 in Figure 8). The model using KOV5 reasonably reproduced the observed xylene or
10 XYL, except for the Chungnam and Busan regions. The observed ethene (or ETE)
11 concentrations were low (< 0.5 ppb), except for the Chungnam region, where the
12 average of measurements was 2.1 ppb. The model ethene concentration was higher than
13 the observations for the SMA, Kyungbuk, and Busan regions, while it had a large
14 negative bias ($-1.6 \sim -1.3$ ppb) for the Chungnam region. Regarding ISO, one of the
15 most important biogenic VOCs, the model values were larger than the observations by
16 a factor of 2.

17 In summary, underestimated CO and aromatic VOCs are the main features of the
18 model evaluation with aircraft observations, along with underestimated ozone and
19 HCHO. The largest discrepancies occur over the Chungnam region, where large point
20 sources are located on the west coast of South Korea. The detailed statistics over the
21 SMA and Chungnam area can be obtained from the Supporting Information (Table S9-
22 S10).

23 Figure 9 displays the vertical distributions of observed and simulated O_3 and related
24 species over SMA. The shapes of the simulated profile were in agreement with the

1 observations. Particularly, the model accurately reproduced the observed NO₂ profiles
2 though the surface NO₂ is underestimated by -4.2 to -0.8 ppb in SMA (Table 2 and
3 Figure 9b). The underestimation of simulated surface NO₂ is explained by the
4 overestimation of molybdenum converter method; surface concentrations of NO₂ from
5 molybdenum converter is larger than photolytic converter by 13.6% on average and 64%
6 at 4 pm (Figure 10). Although the diurnal pattern of surface NO₂ at 12-20 LT is
7 explained by the overestimation ~~of~~ by measurements using a molybdenum converter,
8 there are still some other possible reasons; 1) the emission ~~factor~~ diurnal profile used in
9 this study was developed for the Los Angeles Basin, which may need to be adjusted for
10 SMA, 2) the uncertainty of HO_x and RO_x radicals from other sources can affect the
11 NO₂ concentrations.

12 However, the simulated O₃ and HCHO had negative biases of 16.4 ppb and 0.73
13 ppb, respectively, persisting from the surface to 2 km. Additionally, the simulated CO
14 underestimated the observations by 40% throughout the vertical layer. While the model
15 TOL and XYL, utilizing KOV5, agreed well with the observations at surface level and
16 had the lowest bias of -0.88 and -0.12 ppb under 2 km, the results using EDV2 and
17 EDV3 substantially underestimated the observations throughout the layer (Supporting
18 information, Table S9). On the other hand, the ~~model-model~~-simulated ETE and ISO
19 overestimated the observations below 1 km over SMA.

20

21 **3.3.2. The ground-based observations**

22 During the KORUS-AQ campaign, Pandora and surface measurements were co-located
23 at ~~the~~ Olympic Park. Figure 10 compares the observed diurnal cycle of Pandora vertical
24 columns and surface concentrations of NO₂ and HCHO with the model simulations.

1 ~~The NO₂ measurements were made using a~~ photolytic converter, ~~was used to measure~~
2 ~~surface NO₂ to minimize positive bias from the~~ providing better accuracy compared to
3 measurement with a molybdenum converter. All emissions reasonably simulated the
4 diurnal patterns of vertical column and surface NO₂ and HCHO concentrations.

5 The surface NO₂ peak appeared at 07 LT in the model and 08 LT in the observations,
6 associated with the increase of traffic and the under-developed convective boundary
7 layer. On the other hand, the Pandora NO₂ column amount increased from 06 LT to 12
8 LT and stayed at that value throughout the afternoon, indicating the increase of NO_x
9 emissions from morning to afternoon. The model-simulated NO₂ columns agreed with
10 those from Pandora in terms of absolute values and diurnal variations. The opposite
11 patterns between surface and column NO₂ were attributed to the change of boundary
12 layer height; NO₂ is concentrated near the surface layer as the mixed layer is shallow
13 in the morning and vertically well mixed during the daytime resulting in low surface
14 NO₂ concentrations (Crawford et al., 2020). On the other hand, vertical column NO₂
15 concentrations show large values in the afternoon due to the ~~consistent~~ continued
16 emission of NO_x.

17 All three emission inventories resulted in simulations that underestimated both
18 column and surface HCHO values by up to -8.5×10^{15} molecules·cm⁻² (-46%) at 7 LT
19 and -0.9 ppbv (-26%) at the surface on average. The underestimations of the model
20 HCHO relative to the Pandora and surface observations are similar to findings from
21 comparisons of the model results with the aircraft data (Figure 9). Therefore, the model
22 VOC performance needs to be investigated at ~~the~~ Olympic Park.

23 The diurnal variations of the model O₃, CO, TOL, and XYL were evaluated against
24 the surface observations at ~~the~~ Olympic Park acquired during the KORUS-AQ

1 campaign (Figure 11). The diurnal pattern and hourly averaged mixing ratio of O₃ were
2 well simulated with the three emission inventories with slight model negative biases.
3 The observed CO was 2.7 times higher than the model on average. Considering the
4 diurnal profile of observed TOL and XYL, KOV5 exhibited smaller negative biases
5 than EDV2 and EDV3, but it still showed negative biases. The model TOL and XYL
6 showed peak concentrations at 08 LT, but the observation had a maximum value at 06
7 LT. The model biases of XYL (-3.7 to -0.6 ppb, -89 to -20%) were much larger than
8 those in TOL at the surface. Our study demonstrates that the improvement of VOC
9 emissions and /chemistry representations in the model is necessary for better
10 simulations of air quality over SMA and South Korea.

11

12 **3.4. The model performances over South Korea for the Local and Transport Cases**

13 Previous studies have used meteorological conditions to classify synoptic patterns that
14 affect air pollutant concentrations (Park et al. 2021; Peterson et al. 2019). In contrast,
15 we defined the Transport and Local cases by comparing model results that used the
16 EDV3 base emission and the EDV3 zero-out-Chinese emission (see Figure 12). The
17 Local case comprises May 4, May 20, June 2, and June 3 (Supporting Information,
18 Figure S12), while the Transport case includes May 25, May 26, and May 31
19 (Supporting Information, Figure S13). The Local (Transport) case in this study
20 generally aligns with the Stagnant and Blocking (Transport) cases in Peterson et al.
21 (2019); the Stagnant and Blocking is the period that a large anticyclone is-was located
22 over South Korea, and the Transport case is the period that South Korea was largely
23 affected by long-range transport of air pollutants by westerly wind. The Local case has
24 a Chinese contribution to O₃ of under 11%, whereas the Transport case has a Chinese

1 contribution to O₃ of over 46%. EDV3 performed better in simulating O₃ for the
2 Transport case compared to EDV2 and KOV5, with a bias of only 2.7 ppb in
3 comparison with the DC-8 airborne observations. In contrast, for the Local case, all
4 emissions had a negative bias ranging from 15.5-18.2 ppb. See the Table S11 and S12
5 in Supporting Information to obtain detailed information of model performances
6 against DC-8 measurements for different cases. Surface concentrations of O₃ at
7 Olympic Park also exhibited enhanced contributions from Chinese anthropogenic
8 emissions for Transport case (Figure S14). This section focuses on the model
9 simulations using EDV3 and its modified versions, EDV3_Ch2, EDV3_Ko2 and
10 EDV3_ChKo2 (doubling Chinese and South Korean CO and VOC emissions).

11 Figure 13 illustrates the biases in the model O₃, CO, and HCHO using EDV3 and
12 its variants relative to DC-8 observations over SMA. The plot highlights differences in
13 biases for the Local and Transport cases. The model O₃ biases were negative, and the
14 absolute values of biases were larger in the Local case than in the Transport case (-20%
15 versus -6%). The model CO biases were also negative, and the absolute values of biases
16 were larger in the Transport case than in the Local case. The model HCHO biases were
17 negative and similar for the two cases, except for a larger discrepancy between model
18 and observation in the Local case than in the Transport case.

19 Doubling Chinese CO and VOC emissions (EDV3_Ch2) only slightly reduced
20 biases in the Local case, whereas doubling South Korean CO and VOC emissions
21 (EDV_Ko2) reduced biases more compared to the EDV3_Ch2 case. Doubling South
22 Korean CO and VOC emissions as well as Chinese CO and VOC emissions (EDV3
23 ChKo2) led to the best results in O₃ and CO for the Local case. For the Transport case,
24 doubling Chinese CO and VOC emissions reduced biases to almost zero for CO and

1 HCHO, but the model O₃ was much overestimated, with 14% positive biases (from an
2 original bias of -6%). Doubling South Korean CO and VOC emissions reduced the
3 biases in O₃ and CO a bit, but overestimated HCHO. The overestimation of O₃ in the
4 Transport ease-period in the EDV3_Ch2 and EDV3_ChKo2 cases can be explained by
5 not only excessive ISO but also overpredicted background O₃ from doubled CO and
6 VOC emissions in China (Supporting information, Table S9-S13). Doubled CO and
7 VOC emissions overestimated O₃ concentrations over the Yellow Sea, which implies
8 that the enhanced background O₃ increase can increase the O₃ level in SMA (Supporting
9 Information, Figure S15) (Kim et al., 2023).

10 Further increasing South Korean CO and VOC emissions in addition to the increase
11 of Chinese CO and VOC emissions led to overestimations of O₃ (20%) and HCHO
12 (33%). These sensitivity tests modifying EDV3 indicate that increases in CO and VOC
13 emissions over South Korea improve the model O₃, CO, and VOC simulations.
14 However, increasing Chinese VOC (and CO) emissions may overestimate the model
15 O₃ for the studied period.

16

17 **4. Discussion: strategy for accurate surface O₃ simulations over urban and** 18 **regional areas in China and South Korea**

19 Due to unprecedentedly rich observational data sets acquired during KORUS-AQ, we
20 investigated the status of O₃ simulations and outlined directions for their improvements
21 in SMA and South Korea. In this section, strategies for the enhanced accuracy of surface
22 O₃ simulations over urban and regional areas in China and South Korea are discussed.
23 The discussion is based on the model simulations incorporating various emission
24 scenarios derived from EDV3. In Figures 14 and 15, diverse emission cases are labeled

1 from C1 to C7. Specifically C1, C2, and C3 correspond to EDV3_ChKo2, EDV3_Ch2,
2 and EDV3_Ko2, respectively. Meanwhile, C4, C5, C6, and C7 represent scenarios
3 involving a 50% reduction in Chinese NO_x emissions, a 50% reduction in Chinese VOC
4 emissions, a simultaneous 50% reduction in both Chinese NO_x and VOC emissions,
5 and a 75% reduction of Chinese NO_x emissions, respectively, as discussed in Kim et al.
6 (2023). Examining various options involving the increase and decrease of NO_x and
7 VOC emissions from C1 to C7 sheds light on the direction for improving O₃ simulations.

8 Figure 14 illustrates the model O₃ and NO₂ biases (%) in each region for all cases
9 based on EDV3 (Supporting Information, Table S14-S15 for details). EDV3
10 demonstrated good performance in simulating O₃ and NO₂ for the NCP, KOR, NEC,
11 and NOC region. The most substantial model O₃ biases were observed in SCG and SEC,
12 with minimal model NO₂ biases. Conversely, the largest model NO₂ biases were found
13 in YRD and PRD, accompanied by modest model O₃ biases. Improvements are needed
14 for model O₃ in SCG, SEC, YRD, and PRD with reasonable NO₂ simulations. For SCG
15 and SEC, the C5 case (50% VOC emission reduction only) exhibited the lowest O₃
16 biases. Doubled Chinese VOC emission case (C1 and C2) in SCG and SEC resulted in
17 increased O₃ biases to ~100%, compared to 66.8% in the EDV3 case. In this study, the
18 anthropogenic VOC emissions were reduced. Further reductions of biogenic VOC
19 emissions as well as anthropogenic emissions need to be explored in the future. For
20 SCG and SEC, a reduction in NO_x emissions also led to a slight decrease in O₃ biases.
21 FNR values for the two regions are about 1.3, which turned out to be still VOC-limited
22 or in a transitional state. For the YRD and PRD regions, first, NO_x emissions need to
23 be reduced to improve NO₂ biases in the model. The case C6 (50% reductions in both
24 NO_x and VOC emissions) yielded the most favorable O₃ and NO₂ simulations. Solely

1 reducing NO_x emissions (as in case C4) increase O₃ biases by ~~256~~-~~367~~% relative to
2 EDV3. The FNR values for YRD and PRD are 0.32 and 0.52, respectively, placing them
3 in the VOC-limited regime (FNR < 1). In general, an increase in Chinese VOC
4 emissions (as observed in cases C1 and C2) resulted in elevated surface ozone levels
5 for all regions, including KOR. For NCP, KOR, NEC, and NOC where the model O₃
6 and NO₂ agree with the observations, reducing VOC proves to be an effective strategy
7 for decreasing surface O₃. The biases of O_x typically follow O₃ biases across cases in
8 all regions except NCP, YRD, PRD, and NOC, which experience high NO_x conditions.
9 Refer to Supporting Information Figure S16 for analysis of O_x along with O₃ across
10 various regions. In these specific regions, a substantial reduction in NO_x levels (as in
11 C4 and C7) resulted in an increase in O₃ bias, while there was a decrease in O_x. Likewise,
12 for reduction of O_x, reducing VOC emissions is more effective way to improve O_x in
13 NCP, YRD, KOR, and NEC (as in case C5) (Supporting Information, Figure S16). In
14 SCG and SEC, the 75% reduction of NO_x (C7) showed the lowest O_x concentrations
15 with the decrease in O₃. However, O₃ was increased despite the lowest O_x, revealing
16 that PRD and NOC is in the NO_x saturated regime.

17 In Figure 15, the model O₃ and NO₂ biases (%) in the 12 mega-cities in China and
18 South Korea are illustrated for all cases. Refer to Supporting Information Table S16 and
19 S17 for specific values. EDV3 showed effective performance in simulating O₃ and NO₂
20 for cities such as Beijing, Tianjin, Hangzhou, SMA, and Xian. The most substantial
21 model O₃ biases were observed in Chengdu and Chongqing, with minimal model NO₂
22 biases. In contrast, the notable model NO₂ biases were identified in Shanghai, Nanjing,
23 Guangzhou, Shenzhen, and Wuhan, accompanied by modest model O₃ biases. For
24 Chengdu and Chongqing, situated roughly in SCG, the C5 case (50% VOC emission

1 reduction only) results in the lowest O₃ biases with decent NO₂ simulations. For
2 Shanghai, Nanjing, Guangzhou, Shenzhen, and Wuhan, case C6 (50% reductions in
3 both NO_x and VOC emissions) produced the most favorable O₃ and NO₂ simulations.
4 Simply reducing NO_x emissions (as in case C4) increase O₃ biases in these cities.
5 Overall, the increase in Chinese VOC emissions (cases C1 and C2) resulted in elevated
6 surface ozone levels ~~as well as O_x~~ for all cities, including SMA with an increase in
7 biases, except for Shanghai. Reduction of only VOC emissions (C5) led to the lowest
8 surface O₃ levels for all cities. [The biases of O_x generally follow O₃ biases in Chengdu
9 and Chongqing, where the simulated O₃ initially exhibits a notably high positive bias
10 \(50-60%\), attributable to high VOC. Refer to Supporting Information Figure S17 for an
11 analysis of O_x and O₃ across cases and cities. In contrast, for other cities experiencing
12 high NO_x conditions with positive NO₂ biases, a reduction in NO_x levels \(as in C4 and
13 C7\) led to a decrease in O_x \(and its bias for most cities\). However, there was a
14 simultaneous increase in O₃ and its bias, attributed to the NO_x-saturated regime \(Figure
15 S17\). Likewise, VOC reductions \(as in case C5\) led to O_x reductions more effectively
16 than the case C4 \(50% NO_x reduction\) in all cities except Beijing and Tianjin because
17 of their chemical regime is in the VOC-limited regime \(Supporting Information, Figure
18 S17\).](#)

20 **5. Summary and conclusions**

21 We conducted sensitivity tests using WRF-Chem with three different bottom-up
22 emission inventories (EDGAR-HTAP v2, v3, and KORUS v5) to investigate the
23 impacts of different emissions on the simulation of O₃ and precursors in East Asia. This
24 study is the first to use EDGAR-HTAP v3 with WRF-Chem v4.4 and extends the

1 validation domain to the whole of China during the KORUS-AQ campaign period. We
2 extensively evaluated these emission inventories using both ground and aircraft
3 observations in East Asia.

4 The three emission inventories accurately reproduced the diurnal profiles and
5 absolute values of surface O₃ for most subregions in China, except for the SCG and
6 SEC areas. However, discrepancies were observed in the model performance for the
7 MDA8 O₃ concentrations, with poor correlations observed over regions with high
8 HCHO concentrations (south of 30°N) and relatively low ratios of FNR (north of 30°N).
9 The emission inventories reasonably reproduced the spatial distribution of daily surface
10 NO₂ concentrations. However, we found that CO was considerably underestimated by
11 the emission inventories over both China and South Korea.

12 We evaluated the model simulations against vertical profile measurements of O₃,
13 NO₂, CO, HCHO, TOL, XYL, ETE, and ISO from the DC-8 aircraft, as well as surface
14 observations over South Korea. The simulated vertical shapes of O₃, NO₂, CO, HCHO,
15 TOL, XYL, ETE, and ISO agreed well with the DC-8 measurements in the SMA,
16 although negative biases were observed for O₃, CO, TOL, XYL, and HCHO, with the
17 largest discrepancy between the model results and observations in the Chungnam area.
18 When we compared the simulations with the surface in-situ measurements and
19 PANDORA observations at the Olympic Park in Seoul, the model accurately
20 reproduced the diurnal patterns of surface and vertical columns of NO₂ and HCHO.
21 However, we found that the model underestimated TOL and XYL. This underestimation
22 of TOL and XYL is one of the reasons why the model underestimates O₃ concentrations,
23 as VOCs contribute to NO to NO₂ conversions resulting in O₃ production via
24 photochemistry.

1 We also classified the flight tracks into two categories: Local and Transport cases.
2 We found that the negative bias of O₃ was much larger under the Local case than the
3 Transport case. When the increment of CO and VOC emissions in South Korea is taken
4 into account, the biases of O₃ are significantly reduced, indicating the need for local
5 emission adjustments to decrease O₃ bias in South Korea.

6 To improve surface O₃ simulations over China and South Korea using EDV3,
7 lowering VOC emissions are advantageous for SCG and SEC including urban areas
8 like Chengdu and Chongqing. Meanwhile, for YRD and PRD regions, as well as cities
9 such as Shanghai, Nanjing, Guangzhou, Shenzhen, and Wuhan, both NO_x and VOC
10 emissions should be reduced to enhance model performances. Increase~~e~~ing VOC
11 emissions adversely affected the model's accuracy in simulating O₃ in China, leading
12 to increased biases.

13 Our study revealed a consistent overestimation of isoprene over SMA. The
14 uncertainty of biogenic VOC emissions from MEGAN can affect the model O₃
15 performance. Therefore, to achieve more accurate simulations of O₃ in East Asia, it is
16 essential to explore precise representations of both anthropogenic and biogenic VOC
17 emissions.

18

19 **Code and data availability**

20 WRF-Chem source codes are distributed by NCAR
21 (<https://doi:10.5065/D6MK6B4K>). WRF-Chem v4.4 is available in the GitHub (wrf-
22 model, 2022). The exact version of WRF-Chem codes and configuration files are
23 archived at <https://doi.org/10.5281/zenodo.8260026> (Kim et al., 2023). National

1 Centers for Environmental Prediction (NCEP) FNL data can be accessed from Research
2 Data Archive (RDA) (NCEP, 2019). The CAM-~~c~~Chem data for boundary conditions is
3 also obtained from RDA (ACOM, 2019; doi.org/10.5065/CKR4-GP38). The EDGAR-
4 HTAP v2 data can be downloaded in the website
5 (https://edgar.jrc.ec.europa.eu/dataset_htap_v2). The EDGAR-HTAP v3 is archived on
6 Zenodo (Crippa, 2023). The KORUS-AQ data are available ~~in~~-[from](https://www-air.larc.nasa.gov/cgi-bin/ArcView/korusaq) the website
7 (<https://www-air.larc.nasa.gov/cgi-bin/ArcView/korusaq>)
8 ([doi:10.5067/Suborbital/KORUSAQ/DATA01](https://doi.org/10.5067/Suborbital/KORUSAQ/DATA01)). The EDGAR-HTAP v2, v3, and
9 KORUS v5 data including emission processing programs are available at
10 <https://doi.org/10.5281/zenodo.8260026> (Kim et al., 2023).

11

12 **Author contribution**

13 KMK conducted simulations, analysis and wrote the paper. SWK designed this study,
14 secured funding, performed analysis and wrote the paper. SS supported model set-up
15 and contributed to refining the paper. DRB measured VOC data from DC-8. SC
16 acquired ground-based in-situ VOC data at Olympic Park. JHC performed analysis and
17 wrote the paper. ~~LKE~~ and ~~GGPF~~ assisted in setting up the model emissions and
18 discussed about the model performance. AF measured HCHO data from DC-8. JRH
19 measured Pandora data (NO₂, HCHO). JH retrieved PBL height and discussed about
20 the results. JJ acquired NO₂ data at Olympic Park with different methods. AJW acquired
21 NO₂ and O₃ data from DC-8. JHW and QZ provided emissions inventories and related
22 information. All authors reviewed the manuscript.

23

1 **Competing interests**

2 At least one of the (co-)authors is a member of the editorial board of Geoscientific
3 Model Development.

4
5 **Acknowledgements**

6 This work was supported by the National Research Foundation of Korea (NRF) grant
7 funded by the Korea government (MSIT) (No. 2020R1A2C2014131). S.-W. Kim also
8 acknowledges support from NRF-2018R1A5A1024958. All the computing resources
9 are provided by National Center for Meteorological Supercomputer. The National
10 Center for Atmospheric Research (NCAR) is sponsored by the National Science
11 Foundation (NSF) (NNX16AD96G). We would like to express our gratitude to Glen
12 Diskin for generously providing the CO data from the DC-8 aircraft. We also thanks to
13 Andrew Whitehill and Russell Long for providing the HCHO data from Olympic Park.
14 We would also like to thank Meng Li and Brian McDonald for their valuable
15 discussions, which greatly enhanced our understandings.

16

17 **References**

- 18 Ackermann, I. J., Hass, H., Memmesheimer, M., Ebel, A., Binkowski, F. S., and
19 Shankar, U.: Modal aerosol dynamics model for Europe: Development and first
20 applications, *Atmos. Environ.*, 32, 2981-2999, [https://doi.org/10.1016/S1352-](https://doi.org/10.1016/S1352-2310(98)00006-5)
21 [2310\(98\)00006-5](https://doi.org/10.1016/S1352-2310(98)00006-5), 1998.
- 22 Ahmadov, R., McKeen, S. A., Robinson, A. L., Bahreini, R., Middlebrook, A. M., de
23 Gouw, J. A., Meagher, J., Hsie, E.-Y., Edgerton, E., Shaw, S., and Trainer, M.: A
24 volatility basis set model for summertime secondary organic aerosols over the eastern
25 United States in 2006, *J. Geophys. Res. Atmos.*, 117, D06301,
26 <https://doi.org/10.1029/2011JD016831>, 2012.
- 27 Anenberg, S. C., Henze, D. K., Tinney, V., Kinney, P. L., Raich, W., Fann, N., Malley,
28 C. S., Roman, H., Lamsal, L., Duncan, B., Martin, R. V., van Donkelaar, A., Brauer,
29 M., Doherty, R., Jonson, J. E., Davila, Y., Sudo, K., and Kuylenstierna, J. C.I.:
30 Estimates of the global burden of ambient PM_{2.5}, Ozone, and NO₂ on asthma
31 incidence and emergency room visits, *Environ. Health Perspect.*, 126, 107004,
32 doi.org/10.1289/EHP3766, 2018.

1 Atmospheric Chemistry Observations & Modeling/National Center for Atmospheric
2 Research/University Corporation for Atmospheric Research. 2020. CESM2.1 The
3 Community Atmosphere Model with Chemistry (CAM-chem) Outputs as Boundary
4 Conditions. Research Data Archive at the National Center for Atmospheric Research,
5 Computational and Information Systems Laboratory. [https://doi.org/10.5065/CKR4-](https://doi.org/10.5065/CKR4-GP38)
6 [GP38](https://doi.org/10.5065/CKR4-GP38). Accessed: 16 April 2019.

7 Buchholz, R. R., Emmons, L. K., Tilmes, S., and The CESM2 Development Team,
8 (2019). CESM2.1/CAM-chem Instantaneous Output for Boundary Conditions.
9 UCAR/NCAR - Atmospheric Chemistry Observations and Modeling Laboratory. Lat:
10 -5 to 45, Lon: 75 to 145, 28 Nov 2022, doi.org/10.5065/NMP7-EP60.

11 Carter, W. P.: Documentation of the SAPRC-99 chemical mechanism for VOC
12 reactivity assessment, Contract, 92, 95–308,
13 <https://intra.engr.ucr.edu/~carter/pubs/s99doc.pdf> (last access: 9 June 2023),
14 2000.Chen, S.-H. and Sun, W.-Y.: A one-dimensional time dependent cloud model,
15 *J. Meteorol. Soc. Japan*, 80, 99-118, <https://doi.org/10.2151/jmsj.80.99>, 2002.

16 Choi, J., Henze, D. K., Cao, H., Nowlan, C. R., Abad, G. G., Kwon, H.-A., Lee, H.-M.,
17 Oak, Y. J., Park, R. J., Bates, K. H., Massakkers, J. D., Wisthaler, A., and Weinheimer,
18 A. J.: An Inversion Framework for Optimizing Non-Methane VOC Emissions Using
19 Remote Sensing and Airborne Observations in Northeast Asia During the KORUS-
20 AQ Field Campaign, *J. Geophys. Res. Atmos.*, 127, e2021JD035844,
21 <https://doi.org/10.1029/2021JD035844>, 2022.

22 Colman, J. J., Swanson, A. L., Meinardi, S., Sive, B. C., Blake, D. R., and Rowland, F.
23 S.: Description of the analysis of a wide range of volatile organic compounds in
24 Whole Air Samples collected during PEM-Tropics A and B, *Anal. Chem.*, 73, 3723-
25 3731, <https://doi.org/10.1021/ac010027g>, 2001.

26 Crawford, J. H., Ahn, J.-Y., Al-Saadi, J., Chang, L., Emmons, L. K., Kim, J., Lee, G.,
27 Park, J.-H., Park, R. J., Woo, J. H., Song, C.-K., Hong, J.-H., Hong, Y.-D., Lefer, B.
28 L., Lee, M., Lee, T., Kim, S., Min, K.-E., Yum, S. S., Shin, H. J., Kim, Y.-W., Choi,
29 J.-S., Park, J.S., Szykman, J. J., Long, R. W., Jordan, C. E., Simpson, I. J., Fried, A.,
30 Dibb, J. E., Cho, S., and Kim, Y. P.: The Korea-United States Air Quality (KORUS-
31 AQ) field study, *Elem. Sci. Anth.*, 9, 00163,
32 <https://doi.org/10.1525/elementa.2020.00163>, 2020.

1 Crippa, M., Guizzardi, D., Butler, T., Keating, T., Wu, R., Kaminski, J., Kuenen, J.,
2 Kurokawa, J., Chatani, S., Morikawa, T., Pouliot, G., Racine, J., Moran, M. D.,
3 Klimont, Z., Manseau, P. M., Mashayekhi, R., Henderson, B. H., Smith, S. J.,
4 Suchyta, H., Muntean, M., Solazzo, E., Banja, M., Schaaf, E., Pagani, F., Woo, J.-H.,
5 Kim, J., Monforti-Ferrario, F., Pisoni, E., Zhang, J., Niemi, D., Sassi, M., Ansari, T.,
6 and Foley, K.: The HTAP_v3 emission mosaic: merging regional and global monthly
7 emissions (2000–2018) to support air quality modelling and policies, *Earth Syst. Sci.*
8 *Data*, 15, 2667–2694, <https://doi.org/10.5194/essd-15-2667-2023>, 2023.

9 Crippa Monica. (2023). HTAP_v3 emission mosaic [edgar_HTAPv3_2016_*]. Zenodo.
10 <https://doi.org/10.5281/zenodo.7516361>

11 Dunlea, E. J., Herndon, S. C., Nelson, D. D., Volkamer, R. M., San Martini, F., Sheehy,
12 P. M., Zahniser, M. S., Shorter, J. H., Wormhoudt, J. C., Lamb, B. K., Allwine, E. J.,
13 Gaffney, J. S., Marley, N. A., Grutter, M., Marquez, C., Blanco, S., Cardenas, B.,
14 Retama, A., Ramos Villegas, C. R., Kolb, C. E., Molina, L. T., and Molina, M. J.:
15 Evaluation of nitrogen dioxide chemiluminescence monitors in a polluted urban
16 environment, *Atmos. Chem. Phys.*, 7, 2691-2704, [https://doi.org/10.5194/acp-7-](https://doi.org/10.5194/acp-7-2691-2007)
17 [2691-2007](https://doi.org/10.5194/acp-7-2691-2007), 2007.

18 Emmons, L. K., Walters, S., Hess, P. G., Lamarque, J.-F., Pfister, G. G., Fillmore, D.,
19 Granier, C., Guenther, A., Kinnison, D., Laepple, T., Orlando, J., Tie, X., Tyndall, G.,
20 Wiedinmyer, C., Baughcum, S. L., and Kloster, S.: Description and evaluation of the
21 Model for Ozone and Related chemical Tracers, version4(MOZART-4), *Geosci.*
22 *Model Dev.*, 3, 43-67, <https://doi.org/10.5194/gmd-3-43-2010>, 2010.

23 Emmons, L. K., Schwantes, R. H., Orlando, J. J., Tyndall, G., Kinnison, D., Lamarque,
24 J.-F., Marsh, D., Mills, M. J., Tilmes, S., Bardeen, C., Buchholz, R. R., Conley, A.,
25 Gettelman, A., Garcia, R., Simpson, I., Blacke, D. R., Meinardi, S., and Pétron, G.:
26 The Chemistry Mechanism in the Community Earth System Model version 2
27 (CESM2), *J. Adv. Model. Earth Syst.*, 12, e2019MS001882,
28 <https://doi.org/10.1029/2019MS001882>, 2020.

29 Franklin, B. A., Brook, R., and Arden Pope III, C.: Air Pollution and Cardiovascular
30 Disease, *Curr. Probl. Cardiol.*, 40, 207-238,
31 <https://doi.org/10.1016/j.cpcardiol.2015.01.003>, 2015.

1 Gaubert, B., Emmons, L. K., Raeder, K., Tilmes, S., Miyazaki, K., Arellano Jr., A. F.,
2 Elguindi, N., Granier, C., Tang, W., Barré, J., Worden, H. M., Buchholz, R. R.,
3 Edwards, D. P. Franke, P., Anderson, J. L., Saunois, M., Schroeder, J., Woo, J.-H.,
4 Simpson, I. J., Blake, D. R., Meinardi, S., Wennberg, P. O., Crounse, J., Teng, A.,
5 Kim, M., Dickerson, R. R., He, H., Ren X., Pusede, S. E., and Diskin, G. S.:
6 Correcting model biases of CO in East Asia: impact on oxidant distributions during
7 KORUS-AQ, *Atmos. Chem. Phys.*, 20, 14617–14647, [https://doi.org/10.5194/acp-](https://doi.org/10.5194/acp-20-14617-2020)
8 20-14617-2020, 2020.

9 Goldberg, D. L., Saide, P. E., Lamsal, L. N., de Foy, B., Lu, Z., Woo, J.-H., Kim, Y.,
10 Kim, J., Gao, M., Carmichael, G., and Streets, D. G.: A top-down assessment using
11 OMI NO₂ suggests an underestimate in the NO_x emissions inventory in Seoul, South
12 Korea, during KORUS-AQ, *Atmos. Chem. Phys.*, 19, 1801-1818,
13 <https://doi.org/10.5194/acp-19-1801-2019>, 2019.

14 Grell, G. A.: Prognostic evaluation of assumptions used by cumulus parameterizations,
15 *Mon. Weather Rev.*, 121, 764-787, [https://doi.org/10.1175/1520-](https://doi.org/10.1175/1520-0493(1993)121<0764:PEOAUB>2.0.CO;2)
16 0493(1993)121<0764:PEOAUB>2.0.CO;2, 1993.

17 Grell, G. A. and Dévényi, D.: A generalized approach to parameterizing convection
18 combining ensemble and data assimilation techniques, *Geophys. Res. Lett.*, 29, 38-
19 1-38-4, <https://doi.org/10.1029/2002GL015311>, 2002.

20 Grell, G. A., Peckham, S. E., Schmitz, R., McKeen, S. A., Frost, G., Shamarock, W. C.,
21 and Eder, B.: Fully coupled “online” chemistry within the WRF model, *Atmos.*
22 *Environ.*, 39, 6957-6975, <https://doi.org/10.1016/j.atmosenv.2005.04.027>, 2005.

23 Guenther, A., Karl, T., Harley, P., Wiedinmyer, C., Palmer, P. I., and Geron, C.:
24 Estimates of global terrestrial isoprene emissions using MEGAN (Model of
25 Emissions of Gases and Aerosols from Nature), *Atmos. Chem. Phys.*, 6, 3181-3210,
26 <https://doi.org/10.5194/acp-6-3181-2006>, 2006.

27 Hong, S.-Y. and Noh, Y.: A new vertical diffusion package with an explicit treatment of
28 entrainment processes, *Mon. Weather Rev.*, 134, 2318–2341,
29 <https://doi.org/10.1175/MWR3199.1>. 2006.

30 Jang, Y., Lee, Y., Kim, J., Kim, Y., and Woo, J.-H.: Improvement China point source for
31 improving bottom-up emission inventory, *Asia-Pac. J. Atmos. Sci.*, 56, 107-118,
32 <https://doi.org/10.1007/s13143-019-00115-y>, 2020.

1 Janssens-Maenhout, G., Crippa, M., Guizzardi, D., Dentener, F., Muntean, M., Pouliot,
2 G., Keating, T., Zhang, Q., Kurokawa, J., Wankmüller, R., van der Gon, H. D.,
3 Kuenen J. J. P., Kilmont, Z., Frost, G., Darras, S., Koffi, B., and Li, M.: HTAP_v2.2:
4 a mosaic of regional and global emission grid maps for 2008 and 2010 to study
5 hemispheric transport of air pollution, *Atmos. Chem. Phys.*, 15, 11411-11432,
6 <https://doi.org/10.5194/acp-15-11411-2015>, 2015.

7 Jordan, C. E., Crawford, J. H., Beyersdorf, A. J., Eck, T. F., Halliday, H. S., Vault, B.
8 A., Chang, L.-S., Park, J., Park, R., Lee, G., Kim, H., Ahn, J.-Y., Cho, S., Shin, H. J.,
9 Lee, J. H., Jung, J., Kim, D.-S., Lee, M., Lee, T., Whitehill, A., Szykman, J.,
10 Schueneman, M K., Campuzano-Jost, P., Jimenez, J. L., DiGangi, J. P., Diskin, G. S.,
11 Anderson, B. E., Moore, R. H., Ziemba, L. D., Fenn, M. A., Hair, J. W., Kuehan, R.
12 E., Holz, R. E., Chen, G., Travis, K., Shook, M., Peterson, D. A., Lamb, K. D., and
13 Schwarz, J. P.: Investigation of factors controlling PM_{2.5} variability across the South
14 Korean Peninsula during KORUS-AQ, *Elem. Sci. Anth.*, 8,
15 <https://doi.org/10.1525/elementa.424>, 2020.

16 Jung, J., Lee, J., Kim, B., and Oh, S.: Seasonal variations in the NO₂ artifact from
17 chemiluminescence measurements with a molybdenum converter at a suburban site
18 in Korea (downwind of the Asian continental outflow) during 2015-2016, *Atmos.*
19 *Environ.*, 165, 290-300, <https://doi.org/10.1016/j.atmosenv.2017.07.010>, 2017.

20 Kim, K.-M., Kim, S.-W., Choi, M., Kim, M., Kim J., Shina, I., Kim, J., Chung, C.Y.,
21 Yeo, H., Kim, S.-W., Joo, S. J., MckKeen, S. A., and Zhang, L.: Modeling Asian Dust
22 Storms Using WRF-Chem During the DRAGON-Asia Field Campaign in April 2012,
23 *J. Geophys. Res. Atmos.*, 126, e2021JD034793,
24 <https://doi.org/10.1029/2021JD034793>, 2021.

25 Kim, K.-M., Kim, S.-W., Seo, S., Blake, D. R., Cho, S., Crawford, J. H., Emmons, L.,
26 Fried, A., Herman, J. H., Hong, J., Jung, J., Pfister, G., Weinheimer, A. J., Woo, J.-
27 H., and Zhang, Q.: WRF-Chem configurations and input data sets for sensitivity tests
28 of emission inventories, Zenodo [Data set], <https://doi.org/10.5281/zenodo.8260026>,
29 2023.

30 Kim, S.-W., McDonald, B. C., Baidar, S., Brown, S. S., Dube, B., Ferrare, R. A., Frost,
31 G. J., Harley, R. A., Holloway, J. S., Lee, H.-J., McKeen, S. A., Neuman, J. A., Bowak,
32 J. B., Oetjen, H., Ortega, I., Pollack, I. B., Roberts, J. M., Ryerson, T. B., Scarino, A.

1 J., Senff, C. J., Thalman, R., Trainer, M., Volkamer, R., Wagner, N., Washenfelder, R.
2 A., Waxman, E., and Young, C. J.: Modeling the weekly cycle of NO_x and CO
3 emissions and their impacts on O₃ in the Los Angeles-South Coast Air Basin during
4 the CalNex 2010 field campaign, *J. Geophys. Res. Atmos.*, 121, 1340-1360,
5 <https://doi.org/10.1002/2015JD024292>, 2016.

6 Kim, S.-W., Kim, K.-M., Jeong, Y., Seo, S., Park, Y., and Kim J.: Changed in surface
7 ozone in South Korea on diurnal to decadal timescales for the period of 2001-2021,
8 *Atmos. Chem. Phys.*, 23, 12867-12886, <https://doi.org/10.5194/acp-23-12867-2023>,
9 2023.

10 Kwon, H.-A., Park, R. J., Oak, Y. J., Nowlan, C. R., Janz, S. J., Kowalewski, M. G.,
11 Fried, A., Walega, J., Bates, K. H., Choi, J., Blake, D. R., Wisthaler, A., and Woo, J.-
12 H.: Top-down estimates of anthropogenic VOC emissions in South Korea using
13 formaldehyde vertical column densities from aircraft during the KORUS-AQ
14 campaign, *Elem. Sci. Anth.*, 9, 00109, <https://doi.org/10.1525/elementa.2021.00109>,
15 2021.

16 Kurokawa, J. and Ohara, T.: Long-term historical trends in air pollutant emissions in
17 Asia: Regional Emission inventory in ASia (REAS) version 3, *Atmos. Chem. Phys.*,
18 20, 12761-12793, <https://doi.org/10.5194/acp-20-12761-2020>, 2020.

19 Lee, B.-J., Kim, B., and Lee, K.: Air pollution exposure and cardiovascular disease,
20 *Toxicol. Res.*, 30, 71-75, <https://doi.org/10.5487/TR.2014.30.2.071>, 2014.

21 Lee, J. H., Hong, J.-W., Lee, K. M., Hong, J., Velasco, E., Lim, Y., Lee, J., Nam, K.,
22 and Park, J.: Ceilometer monitoring of boundary layer height in Seoul and its
23 application to evaluate the dilution effect on air pollution, *Boundary Layer Meteorol.*,
24 171, 435-455, <https://doi.org/10.1007/s10546-019-00452-5>, 2019.

25 Li, M., Zhang, Q., Streets, D. G., He, K. B., Cheng, Y. F., Emmons, L. K., Huo, H.,
26 Kang, S. C., Lu, Z., Shao, M., Su, H., Yu, X., and Zhang, Y.: Mapping Asian
27 anthropogenic emissions of non-methane volatile organic compounds to multiple
28 chemical mechanisms, *Atmos. Chem. Phys.*, 14, 5617-5638,
29 <https://doi.org/10.5194/acp-14-5617-2014>, 2014.

30 Li, Q., Zhang, L., Wang, T., Tham, Y. J., Ahmadov, R., Xue, L., Zhang, Q., and Zheng,
31 J.: Impacts of heterogeneous uptake of dinitrogen pentoxide and chlorine activation
32 on ozone and reactive nitrogen partitioning: improvement and application of the

1 WRF-Chem model in southern China, *Atmos. Chem. Phys.*, 16, 14875–14890,
2 <https://doi.org/10.5194/acp-16-14875-2016>, 2016.

3 Liu, Z., Doherty, R. M., Wild, O., Hollaway, M., and O'Connor, F. M.: Contrasting
4 chemical environments in summertime for atmospheric ozone across major Chinese
5 industrial regions: the effectiveness of emission control strategies, *Atmos. Chem.*
6 *Phys.*, 21, 10689-10706, <https://doi.org/10.5194/acp-21-10689-2021>, 2021.

7 Lu, K. D., Hofzumahaus, A., Holland, F., Bohn, B., Brauers, T., Fuchs, H., Hu, M.,
8 Häsel, R., Kita, K., Kondo, Y., Li, X., Lou, S. R., Oebel, A., Shao, M., Zheng, J.
9 M., Wahner, A., Zhu, T., Zhang, T. H., and Rohrer, F.: Missing OH source in a
10 suburban environment near Beijing: observed and modelled OH and HO₂
11 concentrations in summer 2006, *Atmos. Chem. Phys.*, 13, 1057-1080,
12 doi.org/10.5194/acp-13-1057-2013, 2013.

13 Madronich, S.: Photodissociation in the Atmosphere, 1, actinic flux and the effects of
14 ground reflections and clouds, *J. Geophys. Res. Atmos.*, 92, 9740–9752.
15 <https://doi.org/10.1029/JD092iD08p09740>, 1987.

16 Manning, W. J. and von Tiedemann, A. Climate change: Potential effects of increased
17 atmospheric carbon dioxide (CO₂), ozone (O₃), and ultraviolet-B (UV-B) radiation
18 on plant diseases, *Environ. Pollut.*, 88, 219-245, [https://doi.org/10.1016/0269-](https://doi.org/10.1016/0269-7491(95)91446-R)
19 [7491\(95\)91446-R](https://doi.org/10.1016/0269-7491(95)91446-R), 1995.

20 Miyazaki, K., Sekiya, T., Fu, D., Bowman, K. W., Kulawik, S. S., Sudo, K., Walker, T.,
21 Kanaya, Y., Takigawa, M., Ogochi, K., Eskes, H., Boersma, K. F., Thompson, A. M.,
22 Gaubert, B., Barre, J., and Emmons, L. K.: Balance of Emission and Dynamical
23 Controls on Ozone During the Korea-United States Air Quality Campaign From
24 Multiconstituent Satellite Data Assimilation, *J. Geophys. Res. Atmos.*, 124, 387-413,
25 <https://doi.org/10.1029/2018JD028912>, 2019.

26 National Centers for Environmental Prediction/National Weather Service/NOAA/U.S.
27 Department of Commerce. 2000, updated daily. NCEP FNL Operational Model
28 Global Tropospheric Analyses, continuing from July 1999. Research Data Archive at
29 the National Center for Atmospheric Research, Computational and Information
30 Systems Laboratory. <https://doi.org/10.5065/D6M043C6>. Accessed: 25 March 2019.

31 Park, R. J., Oak, Y. J., Emmons, L. K., Kim, C.-H., Pfister, G. G., Carmichael, G. R.,
32 Saide, P. E., Cho, S.-Y., Kim, S., Woo, J.-H., Crawford, J. H., Gaubert, B., Lee, H.-

1 J., Park, S.-Y., Jo, Y.-J., Gao, M., Tang, B., Stanier, C. O., Shin, S. S., Park, H. Y.,
2 Bae, C., and Kim, E.: Multi-model intercomparisons of air quality simulations for
3 the KORUS-AQ campaign, *Elem. Sci. Anth.*, 9, 00139,
4 <https://doi.org/10.1525/elementa.2021.00139>, 2021.

5 Peterson, D. A., Hyer, E. J., Han, S.-O., Crawford, J. H., Park, R. J., Holz, R., Kuehn,
6 R. E., Eloranta, E., Knote, C., Jordan, C. E., and Lefer, B. L.: Meteorology
7 influencing springtime air quality, pollution transport, and visibility in Korea, *Elem.*
8 *Sci. Anth.*, 7, 57, <https://doi.org/10.1525/elementa.395>, 2019.

9 Richter, D., Weibring, P., Walega, J. G., Fried, A., Supler, S. M., and Taubman, M. S.:
10 Compact highly sensitive multi-species airborne mid-IR spectrometer, *Appl. Phys. B*,
11 119, 119-131, <https://doi.org/10.1007/s00340-015-6038-8>, 2015.

12 Rosenzweig, C., Karoly, D., Vicarelli, M., Neofotis, P., Wu, Q., Casassa, G., Menzel,
13 A., Root, T. L., Estrella, N., Seguin, B., Tryjanowski, P., Liu, C., Rawlins, S., and
14 Imeson, A.: Attributing physical and biological impacts to anthropogenic climate
15 change, *Nature*, 453, 353-357, <https://doi.org/10.1038/nature06937>, 2008.

16 Saikawa, E., Kim, H., Zhong, M., Avramov, A., Zhao, Y., Janssens-Maenhout, G.,
17 Kurokawa, J.-I., Klimont, Z., Wagner, F., Naik, V., Horowitz, L. W., and Zhang, Q.:
18 Comparison of emissions inventories of anthropogenic air pollutants and greenhouse
19 gases in China, *Atmos. Chem. Phys.*, 17, 6393-6421, [https://doi.org/10.5194/acp-17-](https://doi.org/10.5194/acp-17-6393-2017)
20 6393-2017, 2017.

21 Sharma, A., Ojha, N., Pozzer, A., Mar, K. A., Beig, G., Lelieveld, J., and Gunthe, S. S.:
22 WRF-Chem simulated surface ozone over south Asia during the pre-monsoon:
23 effects of emission inventories and chemical mechanisms, *Atmos. Chem. Phys.*, 17,
24 14393-14414, <https://doi.org/10.5194/acp-17-14393-2017>, 2017.

25 Sicard, P., Crippa, P., De Marco, A., Castruccio, S., Giani, P., Cuesta, J., Paoletti, E.,
26 Feng, Z., and Anav, A.: High spatial resolution WRF-Chem model over Asia: Physics
27 and chemistry evaluation, *Atmos. Environ.*, 244, 118004,
28 <https://doi.org/10.1016/j.atmosenv.2020.118004>, 2021.

29 Souri, A. H., Nowlan, C. R., Abad, G. G., Zhu, L., Blake, D. R., Fried, A., Weinheimer,
30 A. J., Wisthaler, A., Woo, J.-H., Zhang, Q., Chan Miller, C. E., Liu, X., and Chance,
31 K.: An inversion of NO_x and non-methane volatile organic compound (NMVOC)
32 emissions using satellite observations during the KORUS-AQ campaign and

1 implications for surface ozone over East Asia, *Atmos. Chem. Phys.*, 20, 9837-9854,
2 <https://doi.org/10.5194/acp-20-9837-2020>, 2020.

3 Spinei, E., Tiefengraber, M., Müller, M., Gebetsberger, M., Cede, A., Valin, L.,
4 Szykman, J., Whitehill, A., Kotsaki, A., Santos, F., Abbuhasan, N., Zhao, X., Fioletov,
5 V., Lee, S. C., and Swap, R.: Effect of polyoxymethylene (POM-H Delrin) off-
6 gassing within the Pandora head sensor on direct-sun and multi-axis formaldehyde
7 column measurements in 2016–2019, *Atmos. Meas. Tech.*, 14, 647-663,
8 <https://doi.org/10.5194/amt-14-647-2021>, 2021.

9 Stockwell, W. R., Kirchner, F., and Kuhn, M.: A new mechanism for regional
10 atmospheric chemistry modeling, *J. Geophys. Res. Atmos.*, 102, 25847-25879,
11 <https://doi.org/10.1029/97JD00849>, 1997.

12 Tang, W., Emmons, L. K., Arellano Jr, A. F., Gaubert, B., Knote, C., Tilmes, S.,
13 Buchholz, R. R., Pfister, G. G., Diskin, G. S., Blake, D. R., Blake, N. J., Meinardi,
14 S., DiGangi, J. P., Choi, Y., Woo, J.-H., He, C., Schroeder, J. R., Suh, I., Lee, H.-J.,
15 Kanaya, Y., Jung, J., Lee, Y., and Kim, D.: Source Contributions to Carbon Monoxide
16 Concentrations During KORUS-AQ Based on CAM-chem Model Applications, *J.*
17 *Geophys. Res. Atmos.*, 124, 2796-2822, <https://doi.org/10.1029/2018JD029151>, 2019.

18 Tewari, M., F. Chen, W. Wang, J. Dudhia, M. A. LeMone, K. Mitchell, M. Ek, G. Gayno,
19 J. Wegiel, and Cuenca, R. H.: Implementation and verification of the unified NOAA
20 land surface model in the WRF model, *20th conference on weather analysis and*
21 *forecasting/16th conference on numerical weather prediction*, pp. 11–15, 2004.

22 Travis, K. R., Crawford, J. H., Chen, G., Jordan, C. E., Nault, B. A., Kim, H., Jimenez,
23 J. L., Campuzano-Jost, P., Dibb, J. E., Woo, J.-H., Kim, Y., Zhai, S., Wang, X.,
24 McDuffie, E. E., Luo, G., Yu, F., Kim, S., Simpson, I. J., Blake, D. R., Chang, L.,
25 and Kim, M. J.: Limitations in representation of physical processes prevent
26 successful simulation of PM_{2.5} during KORUS-AQ, *Atmos. Chem. Phys.*, 22, 7933–
27 7958, <https://doi.org/10.5194/acp-22-7933-2022>, 2022.

28 Wada, A., Matsueda, H., Murayama, S., Taguchi, S., Kamada, A., Nosaka, M., Tsuboi,
29 K., and Sawa, Y.: Evaluation of anthropogenic emissions of carbon monoxide in East
30 Asia derived from the observations of atmospheric radon-222 over the western North
31 Pacific, *Atmos. Chem. Phys.*, 12, 12119–12132, [https://doi.org/10.5194/acp-12-](https://doi.org/10.5194/acp-12-12119-2012)
32 12119-2012, 2012.

1 Wiedinmyer, C., and Emmons, L.: Fire Inventory from NCAR version 2 Fire Emission,
2 Research Data Archive at the National Center for Atmospheric Research,
3 Computational and Information Systems Laboratory, <https://doi.org/10.5065/XNPA->
4 [AF09](https://doi.org/10.5065/XNPA-AF09), 2022. last access: 17 Oct 2023.

5 Wild, O., Prather, M. J., and Akimoto, H.: Indirect long-term global radiative cooling
6 from NO_x Emissions, *Geophys. Res. Lett.*, 28, 1719-1722,
7 <https://doi.org/10.1029/2000GL012573>, 2001.

8 Woo, J.-H., Choi, K.-C., Kim, H. K., Baek, B. H., Jang, M., Eum, J.-H., Song, C. H.,
9 Ma, Y.-I., Sunwoo, Y., Chang, L.-S., and Yoo, S. H.: Development of an
10 anthropogenic emissions processing system for Asia using SMOKE, *Atmos. Environ.*,
11 58, 5-13, <https://doi.org/10.1016/j.atmosenv.2011.10.042>, 2012.

12 wrf-model: WRF, Github [code], <https://github.com/wrf-model/WRF/releases/tag/v4.4>,
13 last access: 18 May 2022.

14 Zhang, Y.-L. and Cao, F.: Fine particulate matter (PM_{2.5}) in China at a city level, *Sci.*
15 *Rep.*, 5, 14884, <https://doi.org/10.1038/srep14884>, 2015.

16 Zhang, Y., Zhang, R., Yu, J., Zhang, Z., Yang, W., Zhang, H., Lyu, S., Wang, Y., Dai,
17 W., Wang, Y., and Wang, X.: Isoprene Mixing Ratios Measured at Twenty Sites in
18 China During 2012–2014: Comparison With Model Simulation, *J. Geophys. Res.*
19 *Atmos.*, 125, e2020JD033523, <https://doi.org/10.1029/2020JD033523>, 2020.

20 Zheng, B., Tong, D., Li, M., Liu, F., Hong, C., Geng, G., Li, H., Li, X., Peng, L., Qi, J.,
21 Yan, L., Zhang, Y., Zhao, H., Zheng, Y., He, K., and Zhang, Q.: Trends in China's
22 anthropogenic emissions since 2010 as the consequence of clean air actions, *Atmos.*
23 *Chem. Phys.*, 18, 14095–14111, <https://doi.org/10.5194/acp-18-14095-2018>, 2018.

24 Zhong, M., Saikawa, E., Liu, Y., Naik, V., Horowitz, L. W., Takigawa, M., Zhao, Y.,
25 Lin, N.-H., and Stone, E. A.: Air quality modeling with WRF-Chem v3.5 in East Asia:
26 sensitivity to emissions and evaluation of simulated air quality, *Geosci. Model Dev.*,
27 9, 1201–1218, <https://doi.org/10.5194/gmd-9-1201-2016>, 2016.

1 **Table List**

2

3 Table 1. The model experiments with different emissions.

4

5 Table 2. Comparison of the ground-based hourly O₃, NO₂, and CO observations with
6 the simulations utilizing EDGAR-HTAP v2 (EDV2) and v3 (EDV3) and KORUS v5
7 (KOV5) in each regional box (unit = ppb). N is the number of samples. R is correlation
8 coefficient.

9

10 Table 3. Comparison of total NO_x, TOL, XYL, biogenic isoprene emissions, and
11 formaldehyde to NO₂ ratio (FNR) for different emission data sets in each regional box.
12 The MEGAN biogenic isoprene emissions are equally applied to all simulations using
13 different emission data. (unit = mol/s for emissions)

14

15 Table 4. Comparison of aircraft-based 1-minute-interval O₃, NO₂, CO, HCHO, TOL,
16 XYL, ETE, and ISO observations with EDV2, EDV3, and KOV5 for all flight cases
17 under 2 km height (unit = ppb). N is the number of samples. R is correlation coefficient.

1 **Figure List**

2

3 Figure 1. The averaged spatial distribution map of the NO, CO, and TOL (toluene + less
4 reactive aromatics) emissions from EDGAR-HTAP v2, v3, and KORUS v5 in May. The
5 boxes represent Northern China (NOC, 38-42°N/106-110°E), Sichuan-Chongqing-
6 Guizhou (SCG, 27-33°N/103-109°E), Pearl River Delta (PRD, 21.5-24°N/112-115.5°E),
7 Southeastern China (SEC, 24-28°N/116-120°E), Yangtze River Delta (YRD, 30-
8 33°N/119-122°E), South Korea (KOR, 34.5-38°N/126-130°E), North China Plain (NCP,
9 34-41°N/113-119°E), and Northeastern China (NEC, 43-47°N/124-130°E). NOC, NEC,
10 and SEC are denoted by blue boxes (non-urban). NCP, SCG, PRD, YRD, and KOR are
11 denoted by red boxes (urban).

12

13 Figure 2. The DC-8 flight paths during the KORUS-AQ campaign period (black) and 6
14 regional boxes (1: Seoul Metropolitan Area (SMA); 2: Yellow Sea; 3: Chungnam; 4:
15 Kyungbuk; 5: Gwangju; 6: Busan) (red).

16

17 Figure 3. Averaged O₃ concentrations from ground-based observations and model
18 simulations over the areas that distinguish urban (red box) and non-urban (green box)
19 region (central plot). Box-averaged diurnal cycle (solid lines) of O₃ and 1/4 of standard
20 deviations (filled area) from observations (black), EDV2 (sky blue), EDV3 (blue), and
21 KOV5 (red) by local time are shown. The results are shown for NOC, SCG, PRD, SEC,
22 YRD, KOR, NCP, and NEC.

23

24 Figure 4. Comparison of (a) the campaign averaged ground-based maximum daily
25 average of 8-hour O₃ (MDA8 O₃) (unit: ppb) observations and WRF-Chem simulations
26 with (d) EDGAR-HTAP v2 (EDV2), (e) v3 (EDV3), (f) KORUS v5 (KOV5) and (g, h,
27 i) the differences between the observations and model results. The sub-regions are
28 presented with red (urban) and green (non-urban) boxes. The scatter plots comparing
29 averaged observations and the three-emission-based WRF-Chem simulations (sky blue;
30 EDV2, blue; EDV3, red; KOV5) are shown in (b) and (c) for Eastern China and South
31 Korea, respectively. (a, d-e) Color-filled circles in (a), (d), (e), and (f) represent the
32 averaged MDA8 O₃ for the whole campaign period (1st May to 10th June).

33

34 Figure 5. The same as Figure 3 except NO₂.

35

36 Figure 6. The same as Figure 4 except daily NO₂ (unit: ppb).

37

1 Figure 7. The same as Figure 4 except daily CO (unit: ppm).

2

3 Figure 8. The mean (bars) and 1/4 of standard deviations (whiskers) of (a) O₃, (b) NO₂,
4 (c) CO, (d) HCHO, (e) TOL, (f) XYL, (g) ethene (ETE), and (h) isoprene (ISO) (unit =
5 ppb) from DC-8 (dark grey), EDV2 (sky blue), EDV3 (blue), and KOV5 (red) for each
6 box are shown, respectively. TOL and XYL are calculated based on Table S8
7 (Supporting Information). The contribution of toluene to TOL and m/p-Xylene + o-
8 Xylene to XYL is represented with light grey bars (e, f). The sampling numbers are
9 represented with magenta color above the plots.

10

11 Figure 9. Vertically averaged (a) O₃, (b) NO₂, (c) CO, (d) HCHO, (e) TOL, (f) XYL, (g)
12 ETE, and (h) ISO from DC-8 (black), EDV2 (sky blue), EDV3 (blue), and KOV5 (red)
13 in SMA under 2 km height above ground level. The 1/2 of standard deviations are
14 represented with black whiskers in each 200m layer. The sample number is presented
15 with magenta color on the right side of the plots.

16

17 Figure 10. The diurnal cycles of vertical columns and surface concentrations of (a) NO₂
18 and (b) HCHO from Pandora spectrometer (column), and ground-based instruments
19 (TEI 42i NO_x analyzer and Aerodyne QCL) at the Olympic Park site (37.5232°N,
20 127.126°E). EDV2 (sky blue), EDV3 (blue), and KOV5 (red) are compared with
21 observations. The WRF-Chem vertical column concentrations are produced by
22 summing all vertical layers.

23

24 Figure 11. Diurnal cycles of surface (a) O₃, (b) CO, (c) TOL, and (d) XYL at the
25 Olympic Park site. EDV2 (sky blue), EDV3 (blue), and KOV5 (red) are compared with
26 the observations. 1/4 of standard deviations are represented with grey shades. The
27 average period is from the 11th May to the 10th June.

28

29 Figure 12. Averaged O₃ (bars) and 1/4 of standard deviations (whiskers) (unit: ppbv)
30 for the 20 DC8 flights (under 2 km height). The observations (grey) are compared with
31 the model results utilizing EDV2 (sky blue), EDV3 (blue), and KOV5 (red). White
32 hatch-filled bars over blue bars are the contribution of Chinese emissions to O₃
33 concentrations obtained from the default and sensitivity model runs with/without
34 Chinese anthropogenic emissions. The Local (5/4,20 and 6/2,3) and Transport
35 (5/25,26,31) cases are shaded with light blue and orange, respectively.

36

37 Figure 13. The biases in (a) the model O₃, (b) CO, and (c) HCHO concentrations (bars)
38 relative to the DC-8 observations under 2 km height over SMA (dark gray: EDV3, red:

1 EDV3 Ch2, blue: EDV3 ChKo2): (left panel) Local and (right panel) Transport case.
2 Fractional differences (%) are shown in the white boxes.

3

4 Figure 14. Comparison of relative biases ((Model-Observation)/Observation, unit=%)
5 of daily O₃ and NO₂ at surface observation sites during the KORUS-AQ campaign
6 period from sensitivity simulation (C1-7) with EDV3 in each region (NCP, SCG, YRD,
7 PRD, KOR, NEC, NOC, and SEC). C1; EDGAR-HTAP v3 with double CO and VOC
8 emission in China and South Korea, C2; EDGAR-HTAP v3 with double CO and VOC
9 emission in China, C3; EDGAR-HTAP v3 with double CO and VOC emission in South
10 Korea, C4; EDGAR-HTAP v3 with 50% NO_x reduction in China, C5; EDGAR-HTAP
11 v3 with 50% VOC reduction in China, C6; EDGAR-HTAP v3 with 50% NO_x and VOC
12 reduction in China, C7; EDGAR-HTAP v3 with 75% NO_x reduction in China.

13

14 Figure 15. Same as Figure 14 except that the region is changed to cities; Beijing (39.4-
15 41.1N, 115.4-117.5E), Tianjin (38.55-40.25N, 116.7-118.1E), Chengdu (30.05-31.5N,
16 103-105E), Chongqing (28.15-32.25N, 105.3-110.2E), Shanghai (30.7-31.5N, 120.85-
17 122E), Hangzhou (29.2-30.6N, 118.3-120.9E), Nanjing (31.2-32.65N, 118.35-119.25E),
18 Guangzhou (22.55-24N, 112.9-114.05E), Shenzhen (22.4-22.9N, 113.7-114.65E),
19 SMA (37.2-37.8N, 126.5-127.3E), Wuhan (29.95-31.4N, 113.65-115.1E), and Xian
20 (33.65-34.75N, 107.65-109.9E).

21

1 **Table 1.** The model experiments with different emissions.

Experiments	Emissions
EDV2	EDGAR-HTAP v2
EDV3	EDGAR-HTAP v3
KOV5	KORUS v5
EDV3_Ch2	EDGAR-HTAP v3 with double CO, VOC emission in China
EDV3_Ko2	EDGAR-HTAP v3 with double CO, VOC emission in South Korea
EDV3_ChKo2	EDGAR-HTAP v3 with double CO, VOC emission in China & South Korea

2

1 **Table 2.** Comparison of the ground-based hourly O₃, NO₂, and CO observations with
2 the simulations utilizing EDGAR-HTAP v2 (EDV2) and v3 (EDV3) and KORUS v5
3 (KOV5) in each regional box (unit = ppb). N is the number of samples. R is correlation
4 coefficient.

Region		¹⁾ NCP	^{1),a)} SCG	¹⁾ YRD	¹⁾ PRD	^{1),b)} KOR (SMA)	^{2),c)} NEC	^{2),d)} NOC	^{2),e)} SEC		
N		190	104	93	68	358 (125)	45	28	43		
O ₃	OBS	Mean	44.5	34.6	38.2	27.9	41.5 (36.6)	40.9	44.3	26.1	
		Mean	32.2	53.5	21.6	27.6	40.5 (31.1)	28.6	39.4	40.8	
	EDV2	Bias	-12.3	18.9	-16.6	-0.3	-1.0 (-5.5)	-12.3	-4.9	14.7	
		R	0.65	0.53	0.62	0.61	0.59 (0.60)	0.48	0.63	0.52	
		Mean	43.4	57.5	35.7	34.7	41.0 (32.6)	35.2	43.7	45.5	
	EDV3	Bias	-1.1	23.0	-2.5	6.8	-0.5 (-4.0)	-5.7	-0.6	19.4	
		R	0.68	0.55	0.66	0.65	0.56 (0.57)	0.63	0.67	0.55	
		Mean	49.0	55.3	41.1	35.7	42.2 (33.1)	37.1	43.8	42.4	
	KOV5	Bias	4.5	20.7	2.8	7.8	0.7 (-3.5)	-3.8	-0.5	16.3	
		R	0.71	0.53	0.65	0.70	0.62 (0.64)	0.62	0.67	0.54	
	NO ₂	OBS	Mean	17.5	13.8	17.1	12.9	23.2 (32.5)	13.5	11.9	9.6
			Mean	25.8	12.7	39.8	22.0	18.8 (29.6)	13.7	12.9	11.0
EDV2		Bias	8.3	-1.0	22.7	9.1	-4.3 (-3.0)	0.2	1.0	1.5	
		R	0.45	0.37	0.38	0.54	0.51 (0.34)	0.49	0.47	0.19	
		Mean	21.8	12.2	30.4	21.0	21.3 (31.8)	11.2	10.3	11.3	
EDV3		Bias	4.3	-1.6	13.3	8.1	-1.9 (-0.8)	-2.3	-1.6	1.7	
		R	0.44	0.34	0.36	0.52	0.49 (0.31)	0.49	0.52	0.22	
		Mean	13.9	7.5	23.5	13.3	17.7 (28.3)	7.0	7.7	7.7	
KOV5		Bias	-3.6	-6.3	6.4	0.3	-5.5 (-4.2)	-6.5	-4.2	-1.9	
		R	0.44	0.37	0.41	0.52	0.51 (0.39)	0.49	0.51	0.26	
CO		OBS	Mean	835	597	694	636	443 (493)	527	579	655
			Mean	373	389	455	282	175 (210)	206	162	258
	EDV2	Bias	-462	-208	-239	-354	-267 (-283)	-321	-417	-397	
		R	0.24	0.20	0.42	0.30	0.31 (0.30)	0.21	0.09	0.18	
		Mean	374	359	535	282	196 (208)	221	162	256	
	EDV3	Bias	-461	-238	-159	-354	-247 (-285)	-306	-417	-398	
		R	0.22	0.19	0.35	0.31	0.26 (0.33)	0.24	0.10	0.25	
		Mean	355	358	475	305	190 (217)	231	176	266	
	KOV5	Bias	-480	-239	-219	-331	-253 (-276)	-296	-404	-388	
		R	0.27	0.21	0.48	0.29	0.35 (0.36)	0.15	0.10	0.13	

5 1) Urban area, 2) Non-urban area

6 a) Sichuan-Chongqing-Guizhou, b) South Korea, c) Northeastern China, d) Northern China, e) Southeastern China

1 **Table 3.** Comparison of total NO_x, TOL, XYL, biogenic isoprene emissions, and
 2 formaldehyde to NO₂ ratio (FNR) for different emission data sets in each regional box.
 3 The MEGAN biogenic isoprene emissions are equally applied to all simulations using
 4 different emission data. (unit = mol/s for emissions)

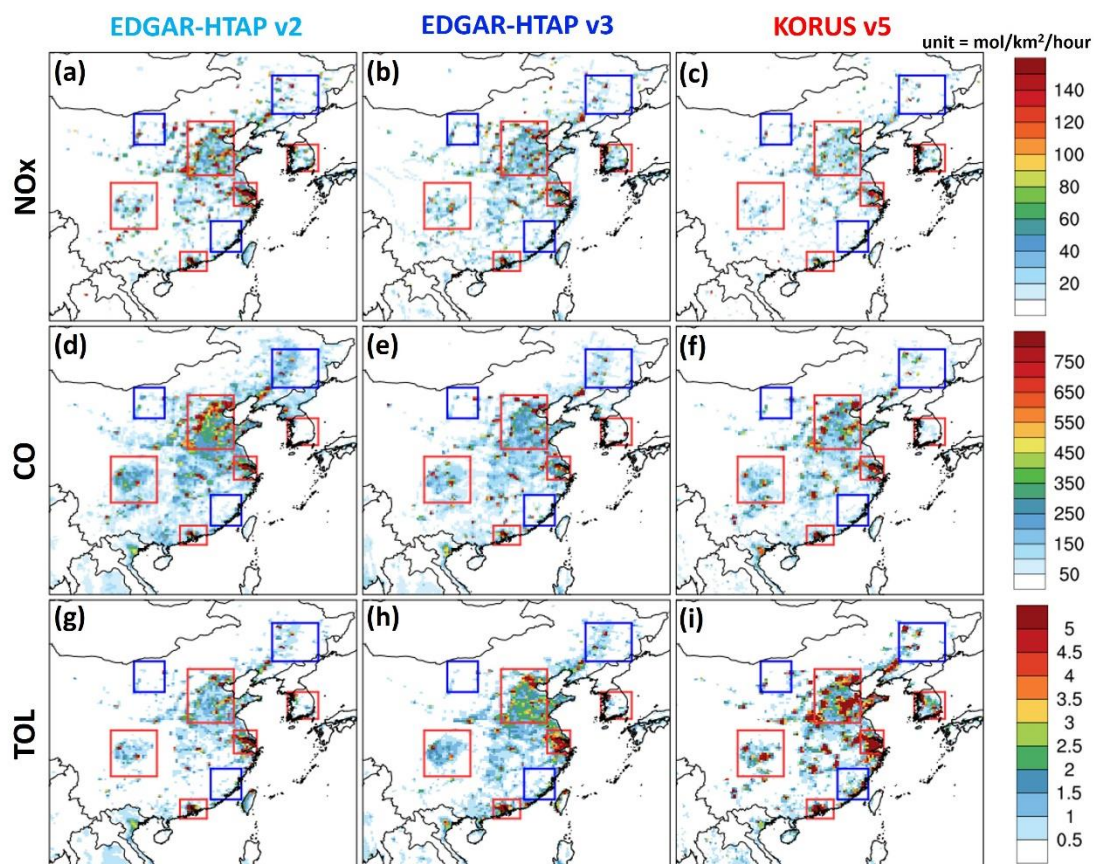
Type	emissions	NCP	SCG	YRD	PRD	KOR(SMA)	NEC	NOC	SEC
NO _x emission	EDV2	5967	1500	2366	1178	990(196)	987	688	590
	EDV3	5202	1654	1642	1091	1191(214)	876	597	662
	KOV5	3237	902	1166	607	886(191)	513	373	410
TOL emission	EDV2	140	56	84	47	27(6)	26	8	20
	EDV3	220	77	99	68	27(8)	40	9	36
	KOV5	403	106	234	155	98(26)	68	21	79
XYL emission	EDV2	84	34	51	28	15(4)	15	4	12
	EDV3	132	46	60	41	16(4)	24	6	22
	KOV5	133	35	79	52	41(9)	21	7	26
Biogenic isoprene emission		132	364	43	127	135(6)	106	23	310
FNR (14- 16LT)	EDV2	0.25	1.31	0.19	0.52	0.53(0.19)	0.68	0.76	1.18
	EDV3	0.44	1.30	0.32	0.52	0.43(0.18)	0.93	0.94	1.33
	KOV5	0.72	2.33	0.48	1.00	0.71(0.22)	1.44	1.49	1.91

5

1 **Table 4.** Comparison of aircraft-based 1-minute-interval O₃, NO₂, CO, HCHO, TOL,
2 XYL, ETE, and ISO observations with EDV2, EDV3, and KOV5 for all flight cases
3 under 2 km height (unit = ppb). N is the number of samples. R is correlation coefficient.

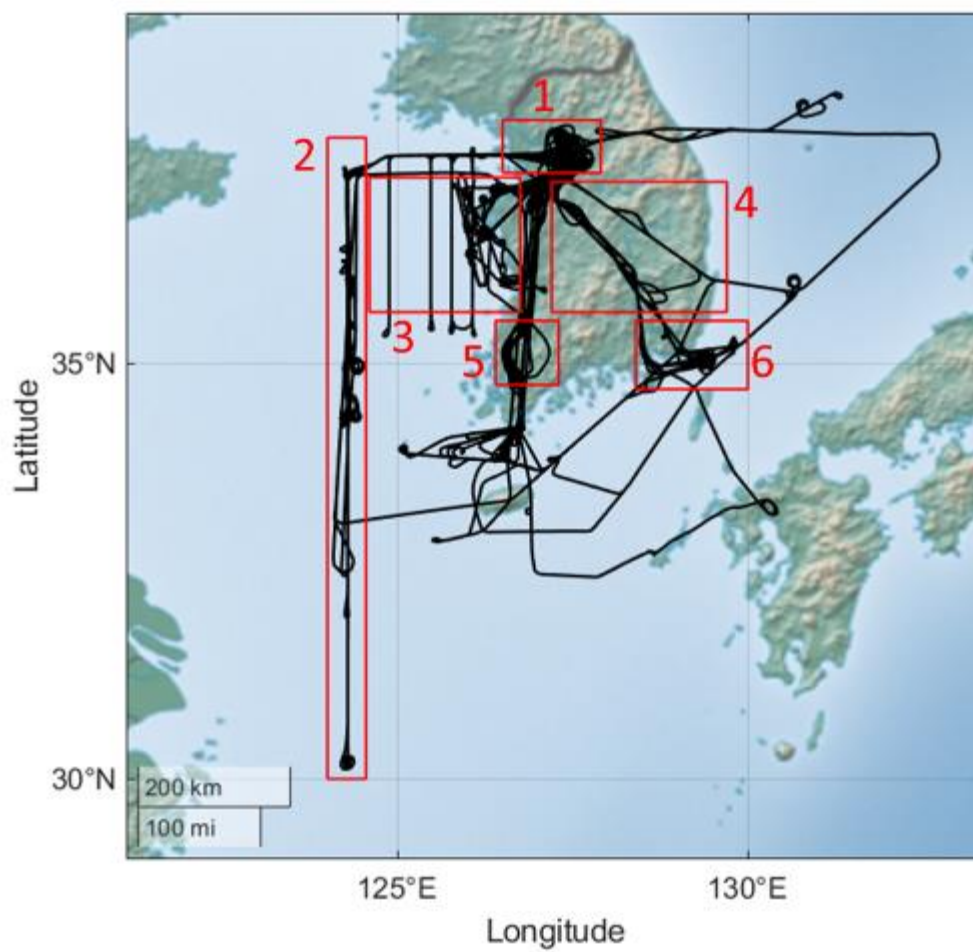
Species	Type	N	Mean	Bias	σ	R
O ₃	OBS	5191	84.4		19.9	
	EDV2		67.5	-16.8	16.7	0.44
	EDV3		69.3	-15.1	17.8	0.43
	KOV5		66.9	-17.5	15.8	0.50
NO ₂	OBS	5047	2.19		4.49	
	EDV2		3.06	0.87	4.60	0.71
	EDV3		3.91	1.72	5.34	0.67
	KOV5		2.83	0.64	4.73	0.73
CO	OBS	5575	253		100	
	EDV2		148	-105	48	0.60
	EDV3		156	-97	47	0.59
	KOV5		146	-107	43	0.62
HCHO	OBS	5365	2.37		1.64	
	EDV2		1.75	-0.62	1.01	0.69
	EDV3		1.78	-0.59	1.02	0.67
	KOV5		1.80	-0.57	1.10	0.71
TOL	OBS	730	2.60		2.02	
	EDV2		0.47	-2.13	0.38	0.39
	EDV3		0.55	-2.05	0.48	0.38
	KOV5		1.58	-1.01	1.30	0.37
XYL	OBS	289	0.73		0.65	
	EDV2		0.23	-0.50	0.23	0.30
	EDV3		0.30	-0.43	0.31	0.30
	KOV5		0.49	-0.24	0.47	0.27
ETE	OBS	2573	0.42		1.59	
	EDV2		0.51	0.09	0.65	0.14
	EDV3		0.56	0.14	0.76	0.15
	KOV5		0.51	0.08	0.58	0.20
ISO	OBS	1294	0.08		0.09	
	EDV2		0.18	0.10	0.21	0.41
	EDV3		0.19	0.11	0.20	0.41
	KOV5		0.17	0.10	0.20	0.42

4

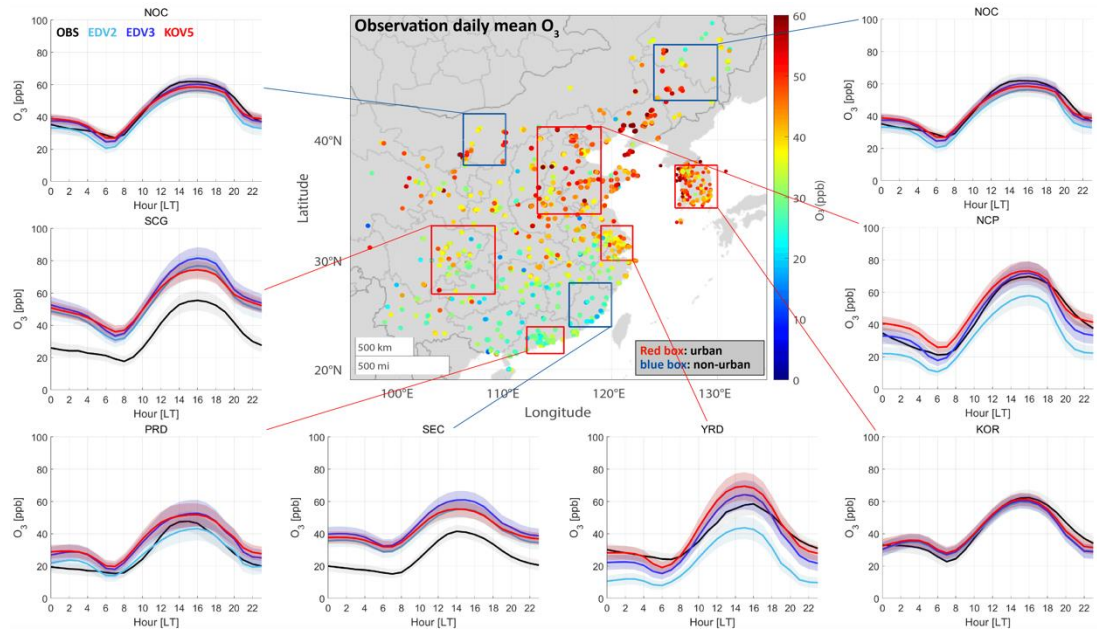


1

2 **Figure 1.** The averaged spatial distribution map of the NO, CO, and TOL (toluene +
 3 less reactive aromatics) emissions from EDGAR-HTAP v2, v3, and KORUS v5 in May.
 4 The boxes represent Northern China (NOC, 38-42°N/106-110°E), Sichuan-Chongqing-
 5 Guizhou (SCG, 27-33°N/103-109°E), Pearl River Delta (PRD, 21.5-24°N/112-115.5°E),
 6 Southeastern China (SEC, 24-28°N/116-120°E), Yangtze River Delta (YRD, 30-
 7 33°N/119-122°E), South Korea (KOR, 34.5-38°N/126-130°E), North China Plain (NCP,
 8 34-41°N/113-119°E), and Northeastern China (NEC, 43-47°N/124-130°E). NOC, NEC,
 9 and SEC are denoted by blue boxes (non-urban). NCP, SCG, PRD, YRD, and KOR
 10 are denoted by red boxes (urban).

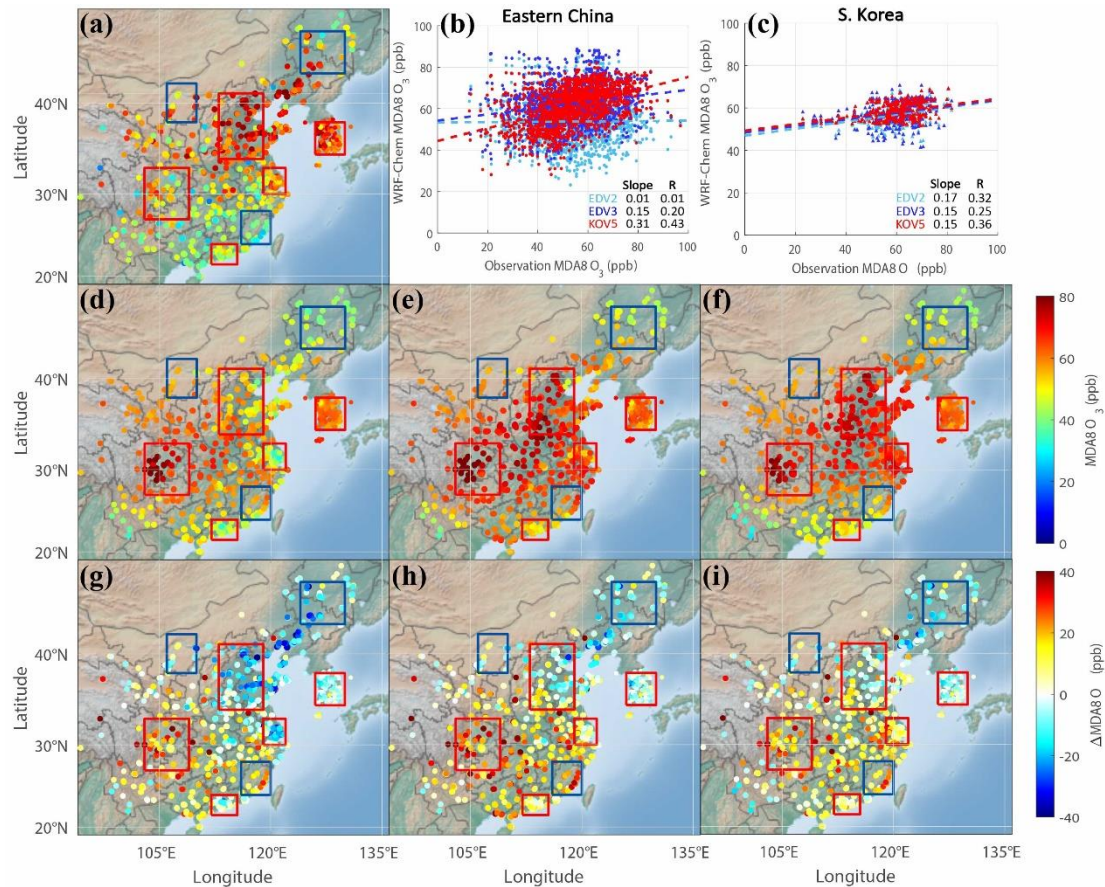


1
 2 **Figure 2.** The DC-8 flight paths during the KORUS-AQ campaign period (black) and
 3 6 regional boxes (1: Seoul Metropolitan Area (SMA); 2: Yellow Sea; 3: Chungnam; 4:
 4 Kyungbuk; 5: Gwangju; 6: Busan) (red).



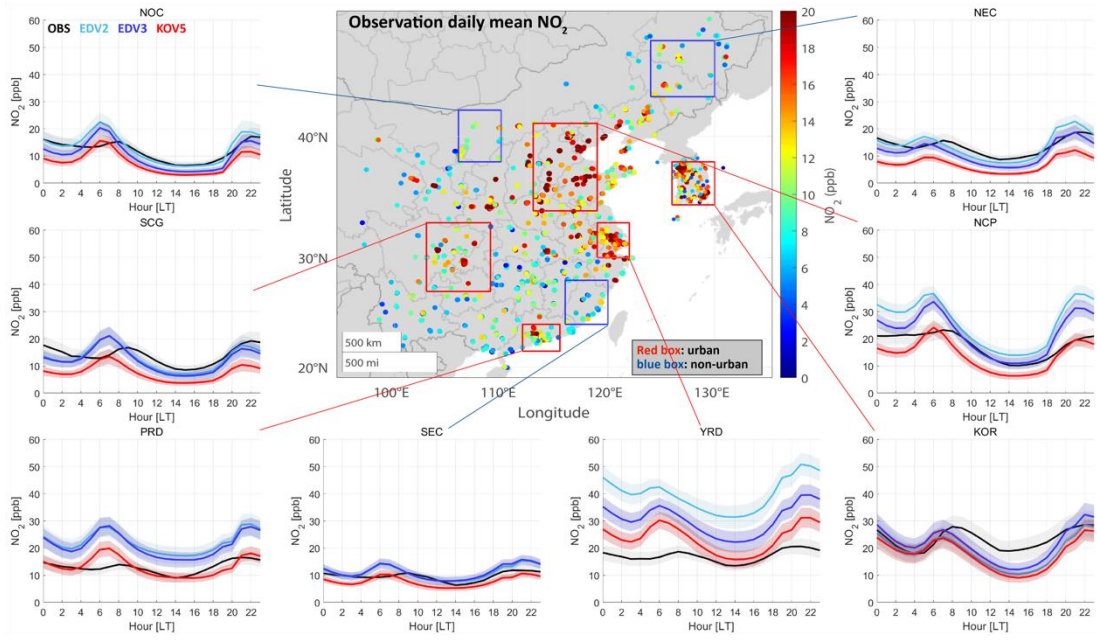
1

2 **Figure 3.** Averaged O₃ concentrations from ground-based observations and model
 3 simulations over the areas that distinguish urban (red box) and non-urban (green box)
 4 region (central plot). Box-averaged diurnal cycle (solid lines) of O₃ and 1/4 of standard
 5 deviations (filled area) from observations (black), EDV2 (sky blue), EDV3 (blue), and
 6 KOV5 (red) by local time are shown. The results are shown for NOC, SCG, PRD, SEC,
 7 YRD, KOR, NCP, and NEC.



1

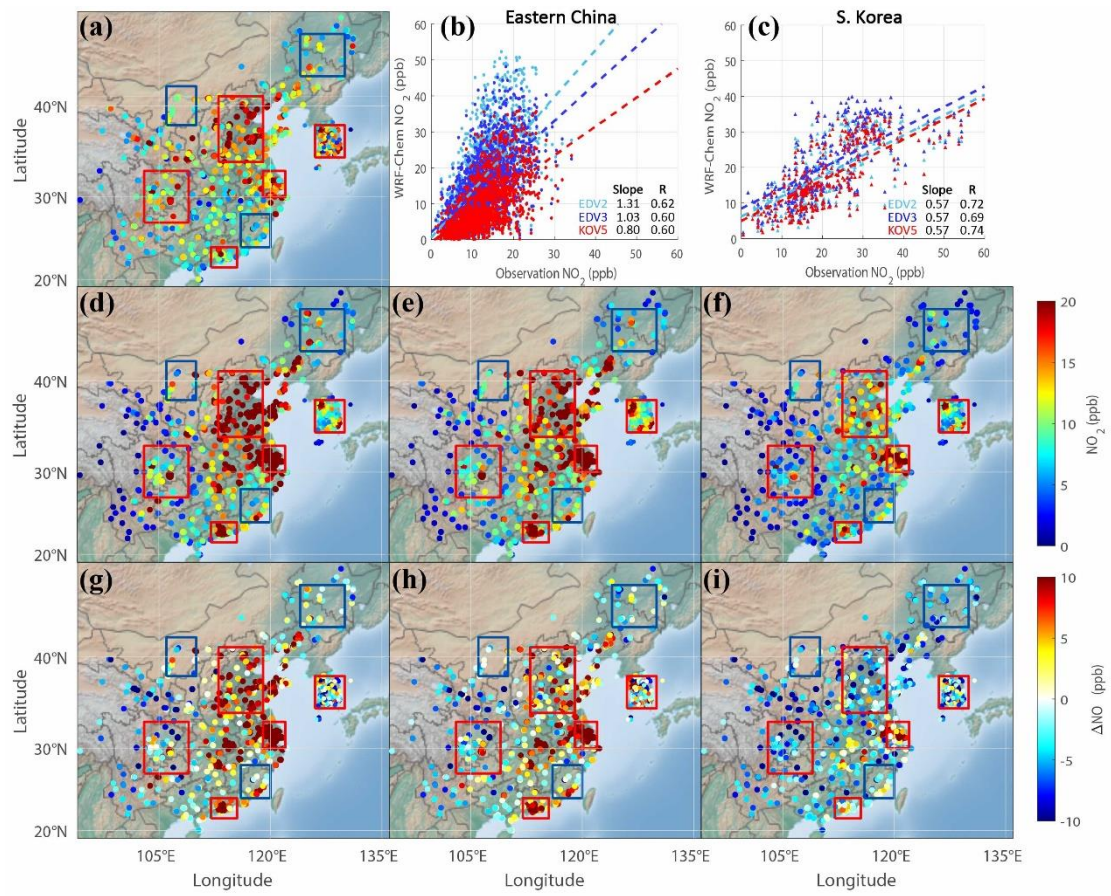
2 **Figure 4.** Comparison of (a) the campaign averaged ground-based maximum daily
 3 average of 8-hour O₃ (MDA8 O₃) (unit: ppb) observations and WRF-Chem simulations
 4 with (d) EDGAR-HTAP v2 (EDV2), (e) v3 (EDV3), (f) KORUS v5 (KOV5) and (g, h,
 5 i) the differences between the observations and model results. The sub-regions are
 6 presented with red (urban) and green (non-urban) boxes. The scatter plots comparing
 7 averaged observations and the three-emission-based WRF-Chem simulations (sky blue;
 8 EDV2, blue; EDV3, red; KOV5) are shown in (b) and (c) for Eastern China and South
 9 Korea, respectively. (a, d-e) Color-filled circles in (a), (d), (e), and (f) represent the
 10 averaged MDA8 O₃ for the whole campaign period (1st May to 10th June).



1

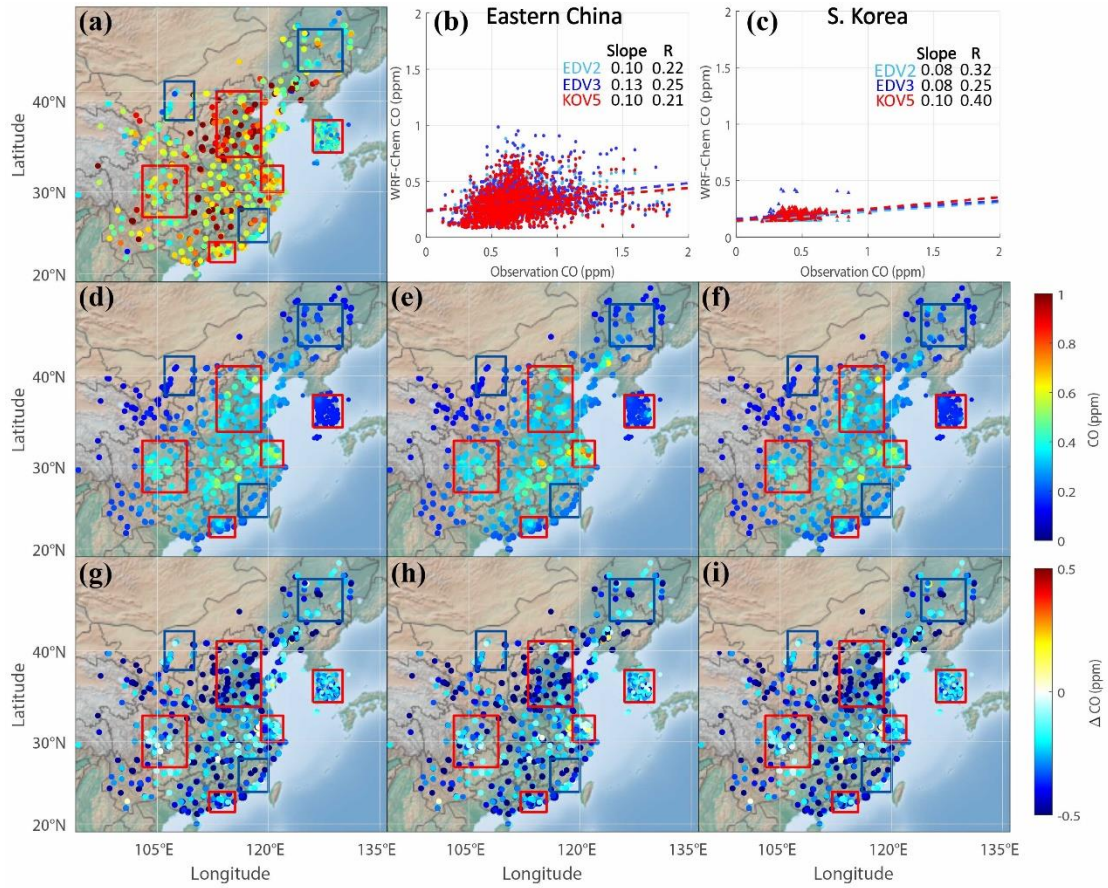
2 **Figure 5.** The same as **Figure 3** except NO_2 .

1



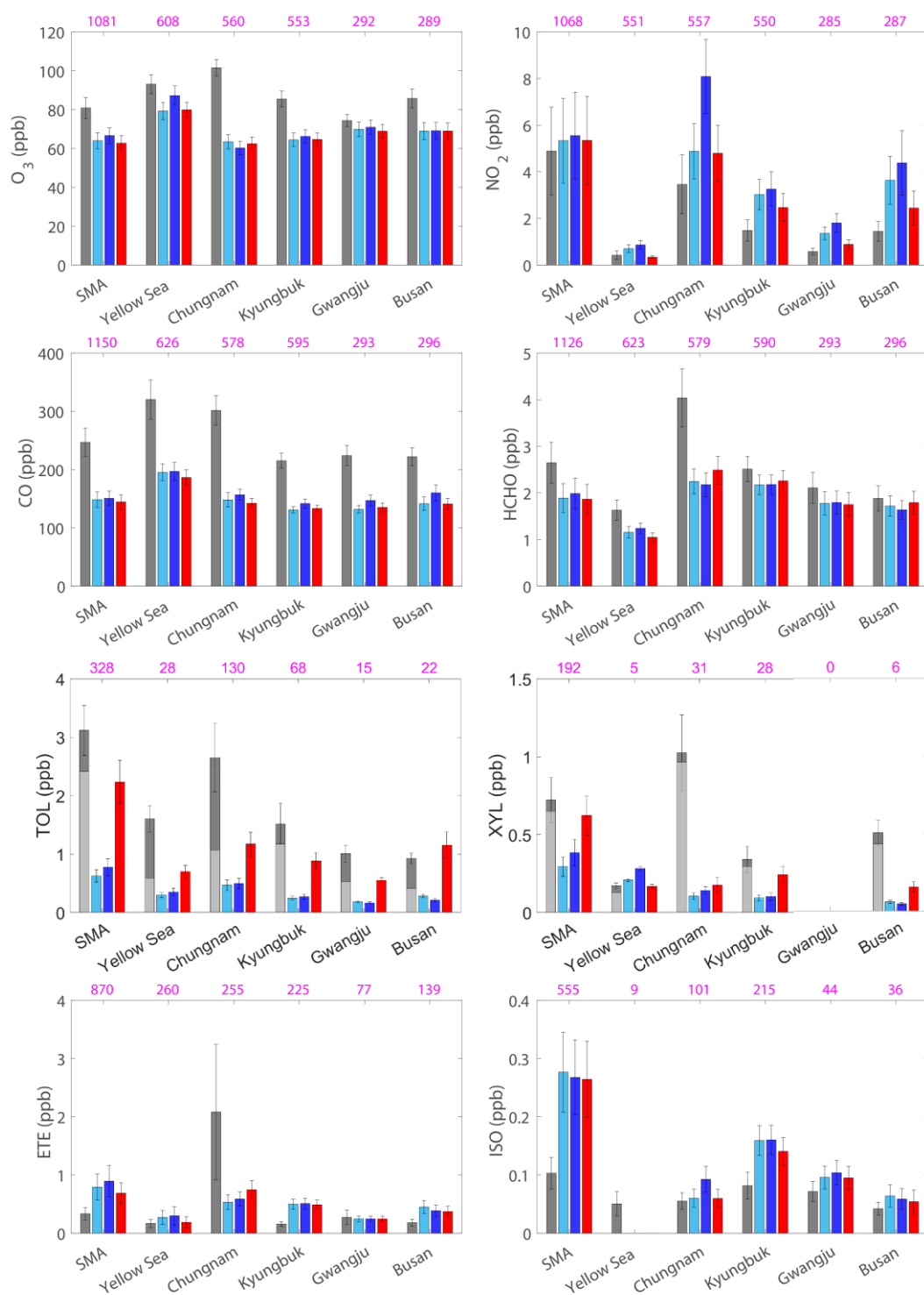
2

3 **Figure 6.** The same as **Figure 4** except daily NO₂ (unit: ppb).



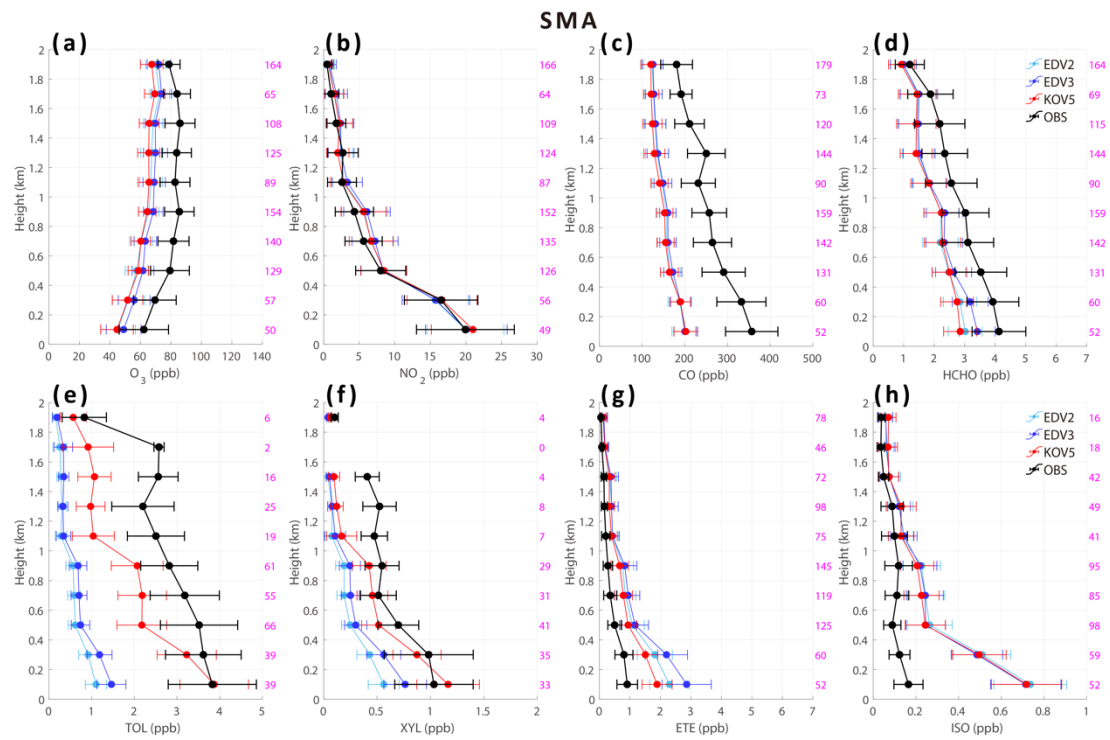
1

2 **Figure 7.** The same as **Figure 4** except daily CO (unit: ppm).



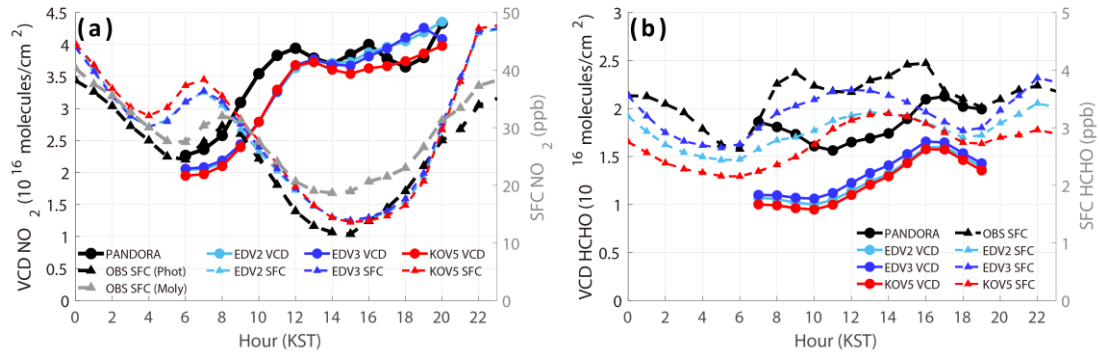
1

2 **Figure 8.** The mean (bars) and 1/4 of standard deviations (whiskers) of (a) O₃, (b) NO₂,
3 (c) CO, (d) HCHO, (e) TOL, (f) XYL, (g) ethene (ETE), and (h) isoprene (ISO) (unit =
4 ppb) from DC-8 (dark grey), EDV2 (sky blue), EDV3 (blue), and KOV5 (red) for each
5 box are shown, respectively. TOL and XYL are calculated based on Table S8
6 (Supporting Information). The contribution of toluene to TOL and m/p-Xylene + o-
7 Xylene to XYL is represented with light grey bars (e, f). The sampling numbers are
8 represented with magenta color above the plots.



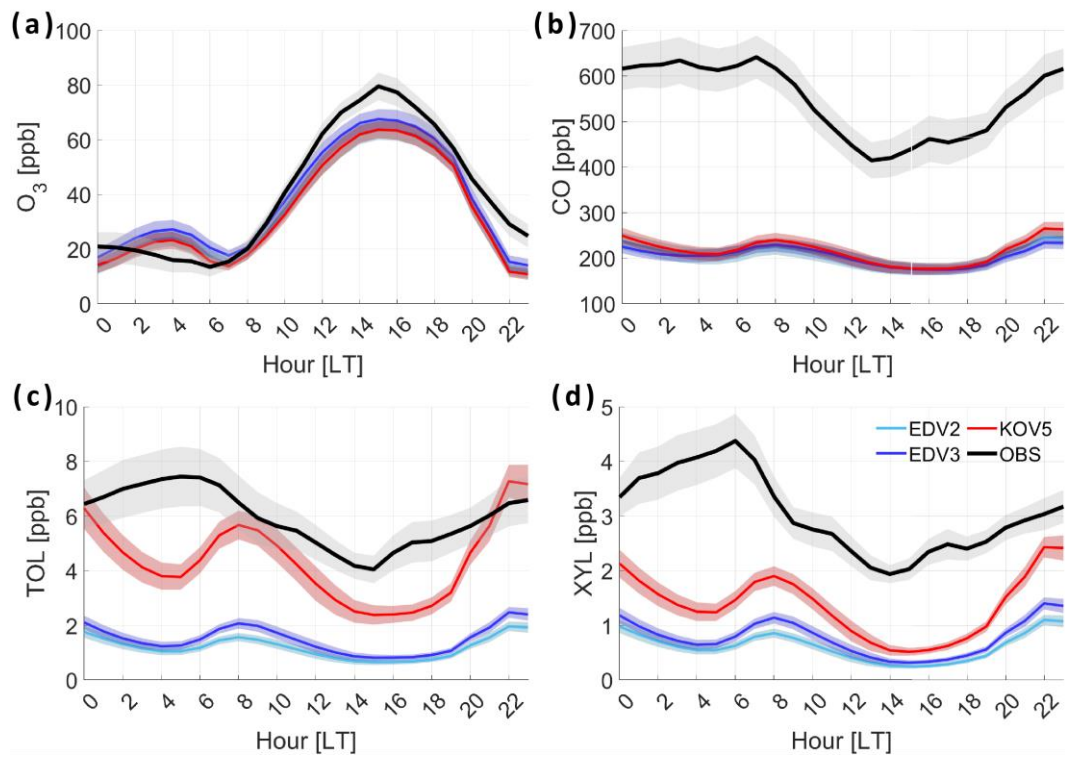
1

2 **Figure 9.** Vertically averaged (a) O_3 , (b) NO_2 , (c) CO, (d) HCHO, (e) TOL, (f) XYL,
 3 (g) ETE, and (h) ISO from DC-8 (black), EDV2 (sky blue), EDV3 (blue), and KOV5
 4 (red) in SMA under 2 km height above ground level. The 1/2 of standard deviations are
 5 represented with black whiskers in each 200m layer. The sample number is presented
 6 with magenta color on the right side of the plots.



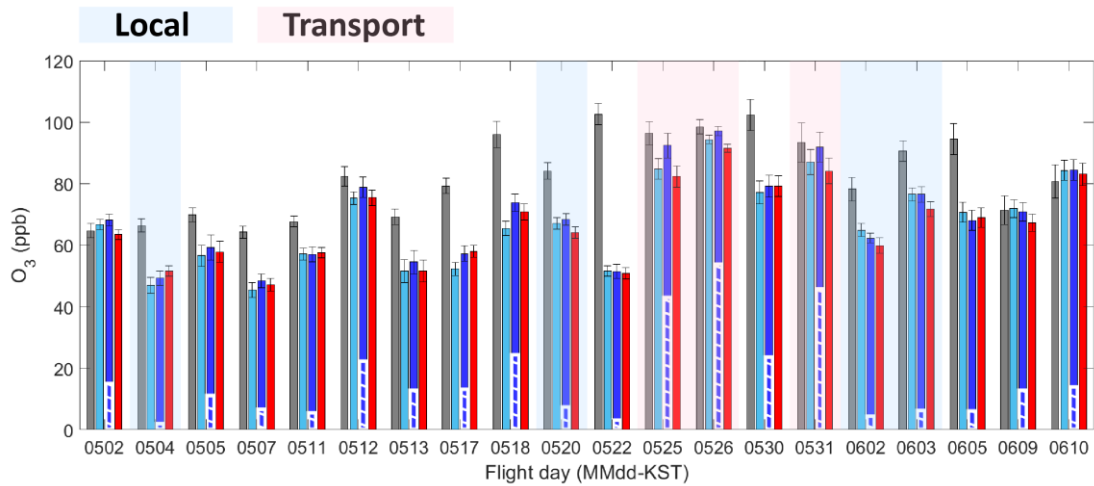
1

2 **Figure 10.** The diurnal cycles of vertical columns and surface concentrations of (a) NO₂
 3 and (b) HCHO from Pandora spectrometer (column), and ground-based instruments
 4 (TEI 42i NO_x analyzer and Aerodyne QCL) at the Olympic Park site (37.5232°N,
 5 127.126°E). Surface concentrations of NO₂ are obtained by the two methods:
 6 molybdenum converter and photolytic method. EDV2 (sky blue), EDV3 (blue), and
 7 KOV5 (red) are compared with observations. The WRF-Chem vertical column
 8 concentrations are produced by summing all vertical layers.



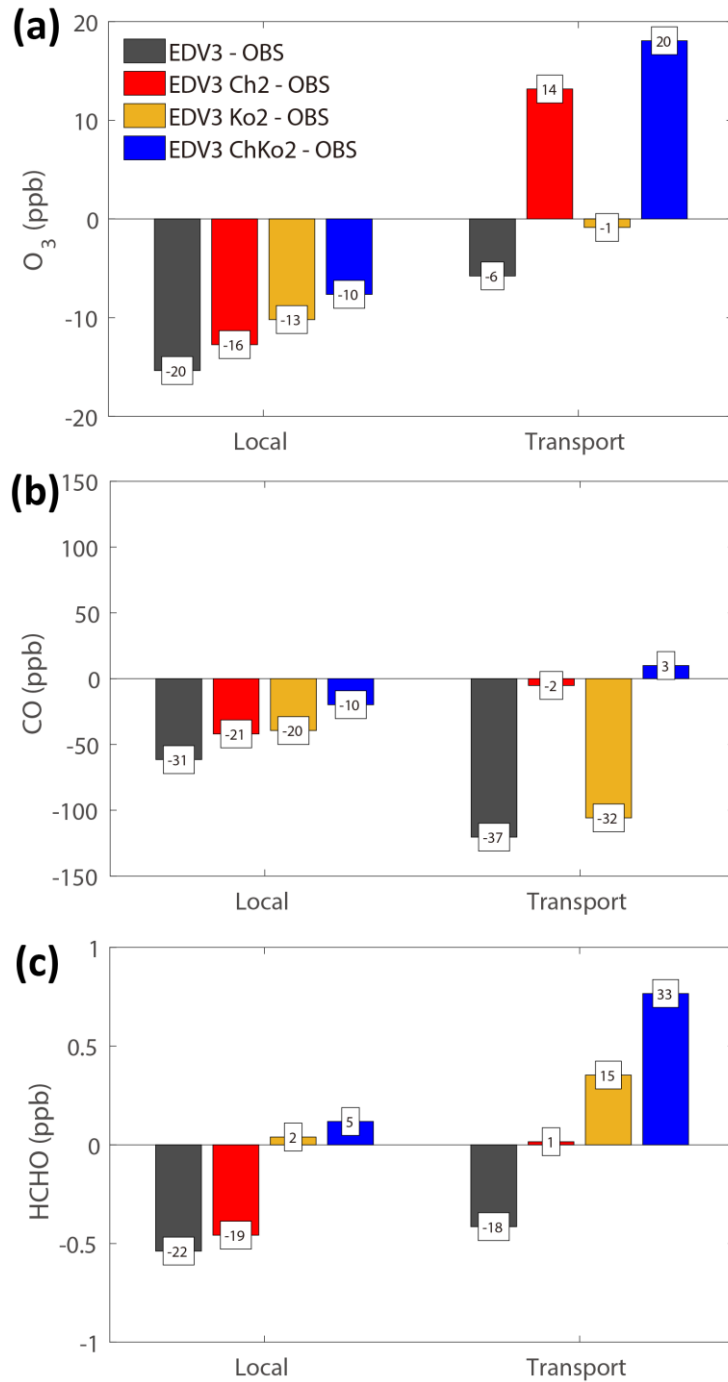
1

2 **Figure 11.** Diurnal cycles of surface (a) O₃, (b) CO, (c) TOL, and (d) XYL at the
 3 Olympic Park site. EDV2 (sky blue), EDV3 (blue), and KOV5 (red) are compared with
 4 the observations. 1/4 of standard deviations are represented with grey shades. The
 5 average period is from the 11th May to the 10th June.



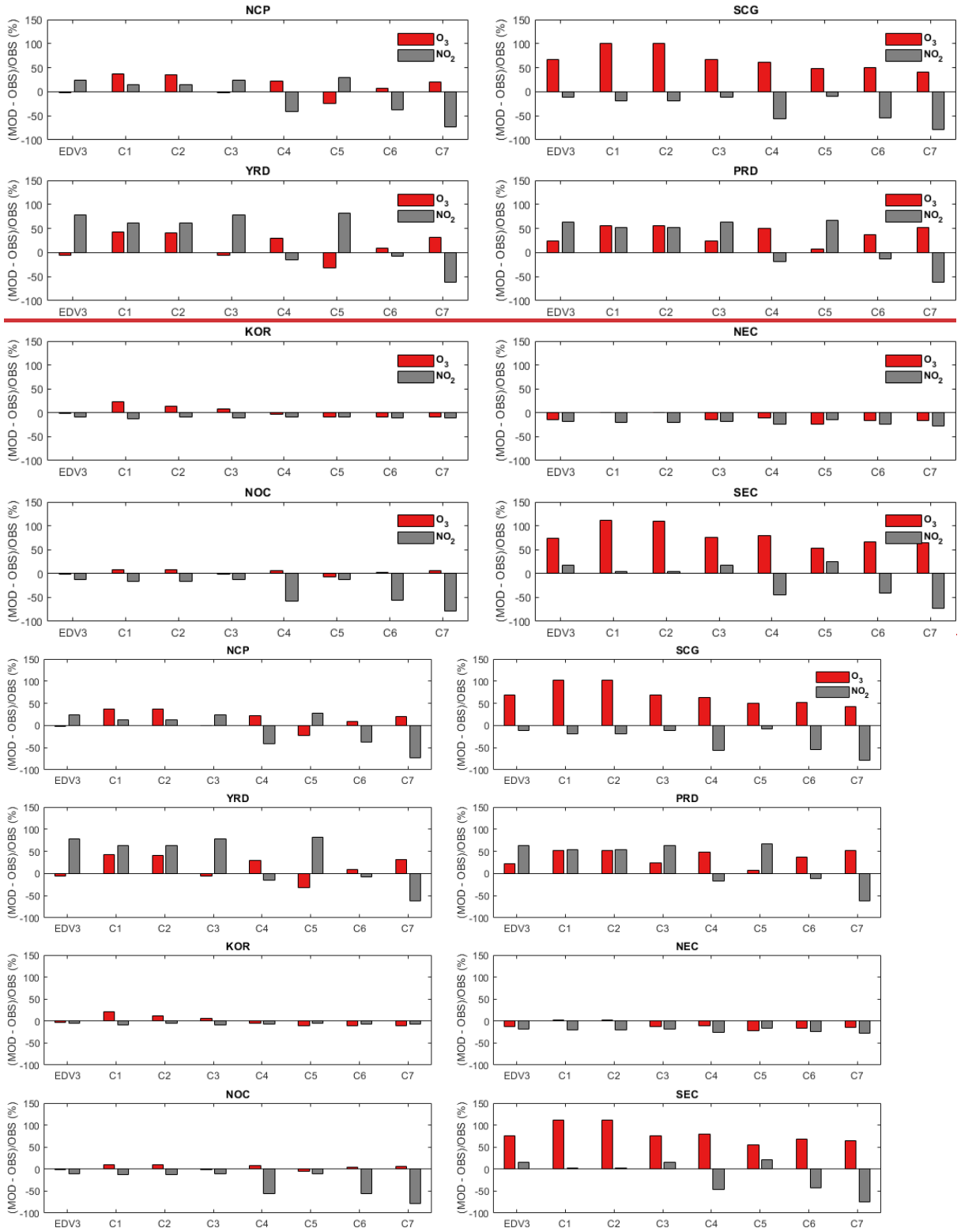
1

2 **Figure 12.** Averaged O_3 (bars) and $1/4$ of standard deviations (whiskers) (unit: ppbv)
 3 for the 20 DC8 flights (under 2 km height). The observations (grey) are compared with
 4 the model results utilizing EDV2 (sky blue), EDV3 (blue), and KOV5 (red). White
 5 hatch-filled bars over blue bars are the contribution of Chinese emissions to O_3
 6 concentrations obtained from the default and sensitivity model runs with/without
 7 Chinese anthropogenic emissions. The Local (5/4,20 and 6/2,3) and Transport
 8 (5/25,26,31) cases are shaded with light blue and orange, respectively.



1

2 **Figure 13.** The biases in (a) the model O₃, (b) CO, and (c) HCHO concentrations (bars)
 3 relative to the DC-8 observations under 2 km height over SMA (dark gray: EDV3, red:
 4 EDV3 Ch2, orange: EDV3 Ko2, red: EDV3_ChKo2): (left panel) Local and (right panel)
 5 Transport case. Fractional differences (%) are shown in the white boxes.

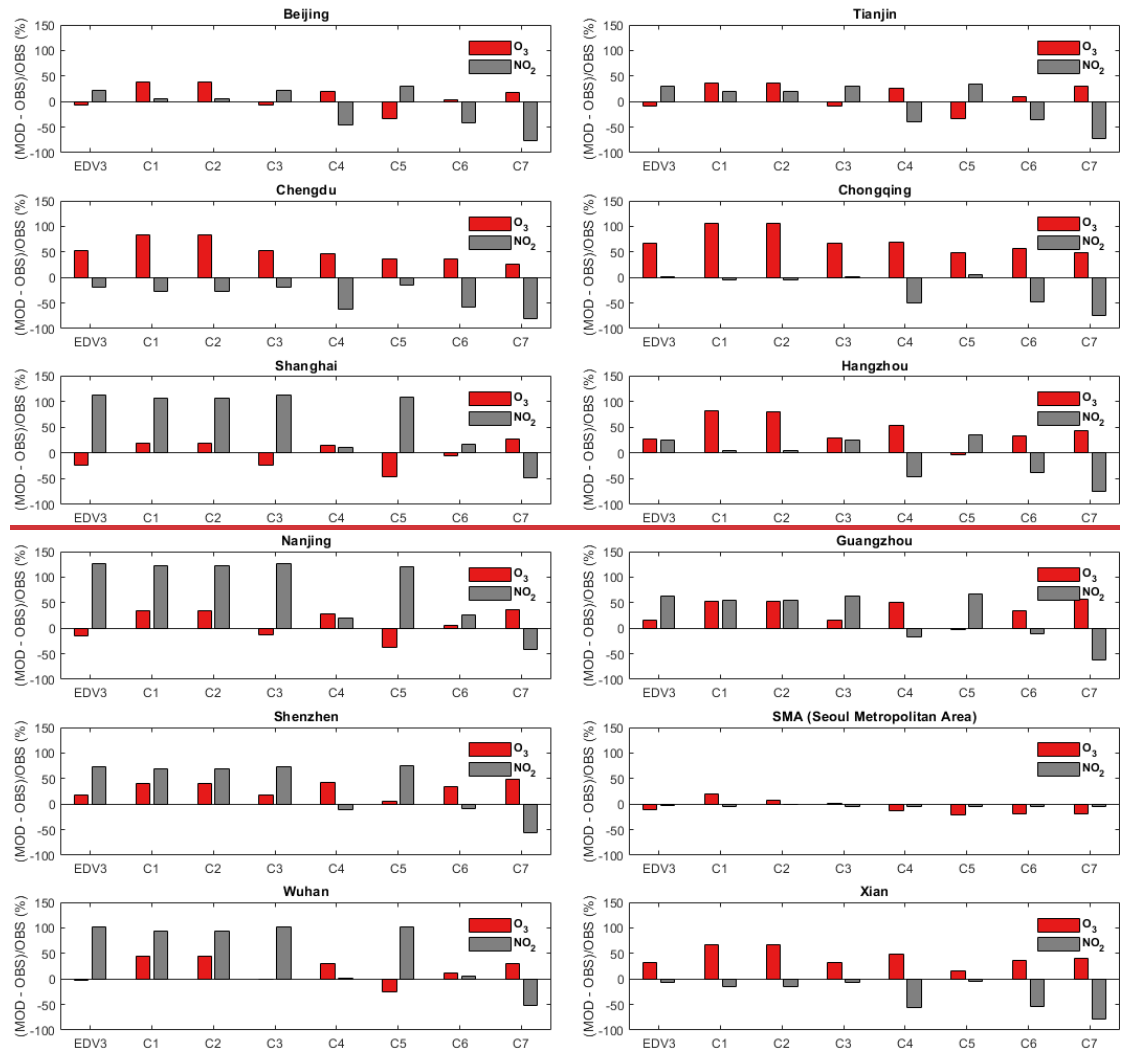


1

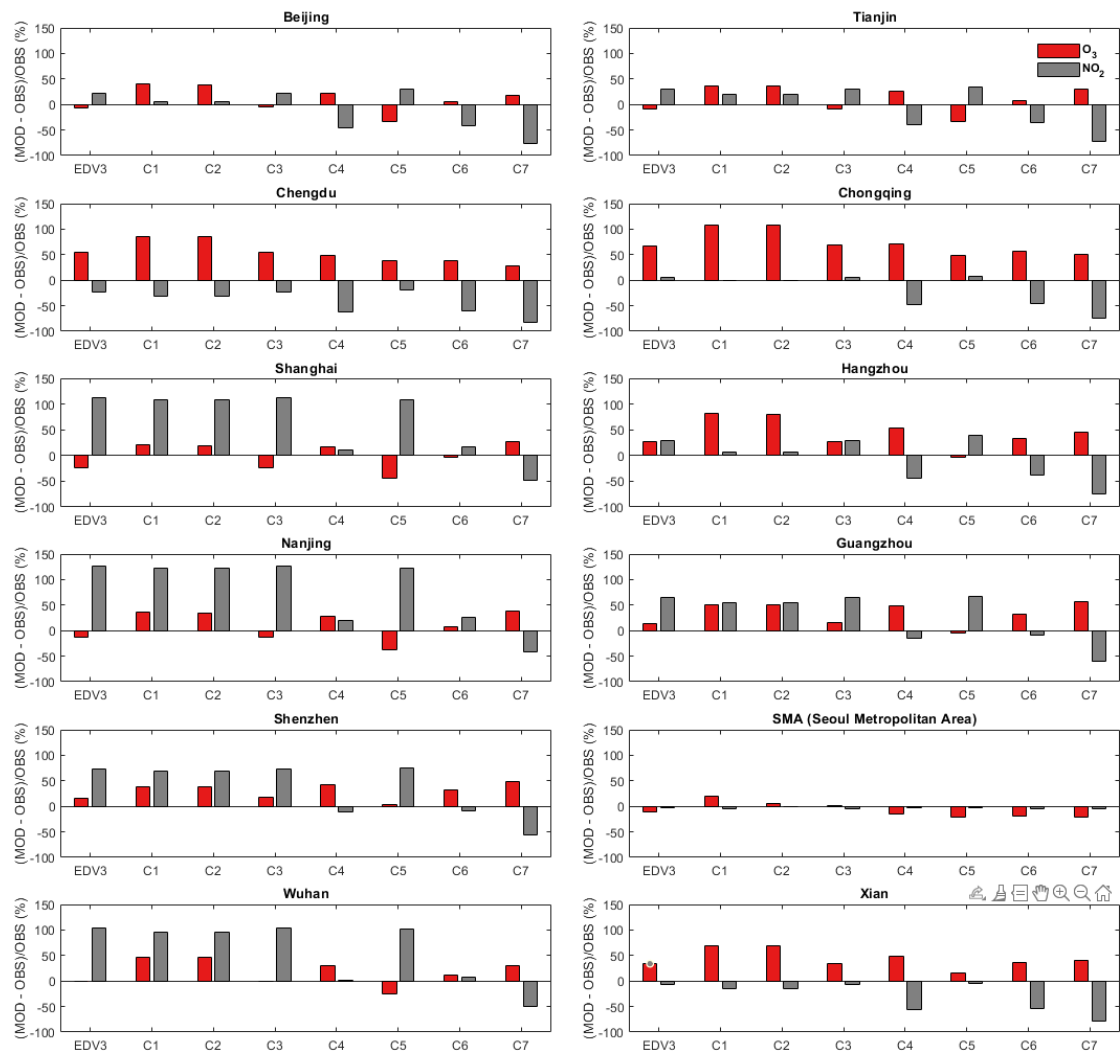
2

3 **Figure 14.** Comparison of relative biases ((Model-Observation)/Observation, unit=%)
 4 of daily O₃ and NO₂ at surface observation sites during the KORUS-AQ campaign
 5 period from sensitivity simulation (C1-7) with EDV3 in each region (NCP, SCG, YRD,
 6 PRD, KOR, NEC, NOC, and SEC). C1; EDGAR-HTAP v3 with double CO and VOC
 7 emission in China and South Korea, C2; EDGAR-HTAP v3 with double CO and VOC

- 1 emission in China, C3; EDGAR-HTAP v3 with double CO and VOC emission in South
- 2 Korea, C4; EDGAR-HTAP v3 with 50% NOx reduction in China, C5; EDGAR-HTAP
- 3 v3 with 50% VOC reduction in China, C6; EDGAR-HTAP v3 with 50% NOx and VOC
- 4 reduction in China, C7; EDGAR-HTAP v3 with 75% NOx reduction in China.



1



1

2 **Figure 15.** Same as **Figure 14** except that the region is changed to cities; Beijing (39.4-
 3 41.1N, 115.4-117.5E), Tianjin (38.55-40.25N, 116.7-118.1E), Chengdu (30.05-31.5N,
 4 103-105E), Chongqing (28.15-32.25N, 105.3-110.2E), Shanghai (30.7-31.5N, 120.85-
 5 122E), Hangzhou (29.2-30.6N, 118.3-120.9E), Nanjing (31.2-32.65N, 118.35-119.25E),
 6 Guangzhou (22.55-24N, 112.9-114.05E), Shenzhen (22.4-22.9N, 113.7-114.65E),
 7 SMA (37.2-37.8N, 126.5-127.3E), Wuhan (29.95-31.4N, 113.65-115.1E), and Xian
 8 (33.65-34.75N, 107.65-109.9E).